PARALLEL ACOUSTIC DELAY LINE (PADL) ARRAYS FOR PHOTOACOUSTIC IMAGING APPLICATIONS

A Dissertation

by

YOUNG CHO

Submitted to the Office of Graduate and Professional Studies of
Texas A&M University
in partial fulfillment of the requirements for the degree of

DOCTOR OF PHILOSOPHY

Chair of Committee,	Jun Zou
Committee Members,	Chin Su
	Jim Ji
	Javier Jo
Head of Department,	Miroslave M. Begovic

December 2017

Major Subject: Electrical Engineering

ABSTRACT

Micromachining process, such as laser micromachining and IC microfabrication process, allows production of complex structures in limited space, which reduces both the size and cost of hardware. In this research, using the advantages of micromachining processes, parallel acoustic delay line (PADL) arrays made of optical fibers and single-crystalline silicon (SCS) have been developed to reduce the number of ultrasonic transducers and data acquisition (DAQ) electronics for real-time photoacoustic tomography (PAT). The PADL arrays allow real-time PAT with the significantly reduced number of ultrasonic transducers and DAQs.

Handheld optical PADL array enables more practical operation for photoacoustic imaging applications by miniaturizing previously developed optical PADL array. Sixteen channels of optical fiber PADLs were fabricated and assembled with laser micromachined acrylic housing for the compact structure. By conducting ultrasonic transmission testing, acoustic properties of optical fibers have been characterized. PA imaging capability of optical fiber PADL array has been evaluated by PA imaging experiment.

Microfabrication process makes it possible to use single-crystalline silicon as a material for acoustic delay lines. Acoustic properties of silicon were characterized by ultrasonic transmission testing. Based on the characterization result, silicon acoustic delay line was designed into a spiral coil shape to minimize the overall size. Silicon PADLs are better than optical fiber PADL for miniaturization due to the advantages of microfabrication process. Silicon PADL array achieved a channel reduction ratio of 16:1,

which is twice the ratio of optical fiber PADL. The PA imaging experiment has demonstrated the PA imaging capability of silicon PADL array.

For fast imaging speed and good spatial resolution, silicon PADL array has been improved by applying 3D-printed linker structures and tapered input terminal. Linker structure design has been evaluated by both structural and acoustic simulation. The final design of linker structure is 3D-printed polymer linker to securely hold silicon delay lines with minimal contacts. Tapered input terminal was designed to reduce acoustic acceptance angle for better spatial resolution. Tapered input terminal was evaluated by acoustic simulation with different designs. Those designs and techniques are expected to provide new solutions to reduce the cost and complexity of ultrasonic receiving systems for photoacoustic imaging applications.

DEDICATION

To my father, mother, brother, and nieces.

ACKNOWLEDGEMENTS

First of all, I would like to express my deepest appreciation to my advisor, Professor Jun Zou, who has the attitude and the substance of a genius: he continually and convincingly conveyed a spirit of adventure in regards to research. I am grateful for his guidance and the opportunities he has given me. Also, he has cheered me up and given me sincere advice as a mentor when I faced difficulties during my degree program. Without his guidance and persistent help, this dissertation would not have been possible. I will forever remember all the great times that I have had in the lab.

I would like to thank my defense committee members, Professor Chin Su, Professor Jim Ji, and Professor Javier Jo. I also recognize and appreciate Professor Xing Cheng and Professor Jun Kameoka for their sincere interest and guidance towards my work.

I would like to thank all of my friends, both in South Korea and in the United States, for their continued support, encouragement, and prayers.

Finally, I would like to express the deepest gratitude to my family for unconditional love. Father, mother, and brother, you have all provided support, encouragement, constant prayers, and interest in my dissertation work. Thank you for listening to my problems and providing advice. I would not be who am I today without you all. I would like to give a special thanks to my lovely nieces, Shinhyeong and Hajin. Their lovely smile and voice always make me smile, even in difficult times during my time preparing for my dissertation.

Last but not least, I would like to thank God for letting me know God and helping me finish my dissertation work under His guidance. Needless to say, meeting God was the most important event in my life, not a doctoral degree. I thank God again for leading me in your truth and righteousness.

CONTRIBUTORS AND FUNDING SOURCES

Contributors

This work was supervised by a dissertation committee consisting of Professor Jun Zou, Professor Chin Su, and Professor Jim Ji of the Department of Electrical and Computer Engineering and Professor Javier Jo of the Department of Biomedical Engineering.

Funding Sources

This work was supported in part by in part by a grant (CMMI-1131758) from the National Science Foundation (NSF), grants (U54- CA136398 and DP1 EB016986) from the National Institutes of Health (NIH), and MSIP (Ministry of Science, ICT, and Future Planning), Korea, under the “IT Consilience Creative Program” (NIPA-2013-H0203-13-1001) supervised by the NIPA (National IT Industry Promotion Agency) and National Research Foundation and NRF grant of Korea government (MSIP) (2011-0030075).

NOMENCLATURE

ADC	Analog-to-Digital Converter
ANSI	American National Standards Institute
DAQ	Data AcQuisition
DOT	Diffuse Optical Tomography
DRIE	Deep Reactive Ion Etching
EM	ElectroMagnetic
GPU	Graphics Processing Unit
JBO	Journal of Biomedical Optics
JMM	Journal of Micromechanics and Microengineering
JOPT	Journal of Optics
Nd:YAG	Neodymium-doped Yttrium Aluminium Garnet
OCT	Optical Coherence Tomography
OPO	Optical Parametric Oscillator
OSC	Oscilloscope
PA	PhotoAcoustic
PACT	PhotoAcoustic Computed Tomography
PAM	PhotoAcoustic Microscopy
PAT	PhotoAcoustic Tomography
PDA	Parallel Data Acquisition
RF	Radio Frequency

SAFT	Synthetic Aperture Focusing Technique
SNR	Signal-to-Noise Ratio
SPIE	International Society for Optics and Photonics
UT	Ultrasonic Transducer

TABLE OF CONTENTS

Page

LIST OF FIGURES

Page

LIST OF TABLES

Page

1. INTRODUCTION

Photoacoustic (PA) effect, also called the optoacoustic effect, was first reported by Alexander Graham Bell in 1880. PA effect is the generation of acoustic waves from an object by electromagnetic (EM) radiation. However, mainly due to the absence of a proper light source, there was little research progress on the PA effect until the 1970s. The fundamental principle of the PA wave generation by PA effect can be described as the following: an object is irradiated by EM source, some of the light from the laser excitation is absorbed by an object, the absorbed energy converts into heat, and the temperature of the object increases. As the temperature increases, thermoelastic expansion, which results in pressure changes, takes place. The pressure changes generate ultrasonic waves, which are referred to as photoacoustic waves. For PA effect, the time-variant heating source is required because a time-invariant heating does not produce acoustic waves.

The advantage of photoacoustic tomography (PAT) is its noninvasive biomedical imaging capability with the ability of cross-sectional or three-dimensional (3D) imaging. However, PAT has been developed as an imaging technology only in the last few decades, and now it can provide high-resolution structural, functional [1], and molecular imaging [2, 3].

1.1 Photoacoustic imaging and biomedical applications

Optical imaging in biomedicine is highly desirable because it is very sensitive to optical absorption in biological tissue which can provide functional information, especially blood in vessels [4, 5] and brain [6-10]. Functional magnetic resonance imaging

(fMRI) can also be used as a functional approach for the brain, but optical imaging can detect brain activities with a fast and direct response to stimulus [7, 11].

However, pure optical imaging, including optical coherence tomography (OCT) [5], confocal microscopy, and two-photon microscopy, has shallow penetration depth in biological tissue due to strong optical scattering. Diffuse optical tomography (DOT) can provide molecular and functional imaging beyond soft depth limit but the spatial resolution is poor. Thus, it has significant drawbacks to image a deep-seated object in scattering biological tissues such as a brain under the skull. It can be imaged with poor spatial resolution due to strong optical scattering in tissues [11], or invasive open-skull imaging can be done [12-15].

Pure ultrasonic imaging can give better spatial resolution than pure optical imaging for deep imaging because ultrasonic scattering is much weaker than the optical scattering. However, ultrasonic imaging can provide only mechanical properties, not functional information which the optical imaging does.

The motivation for PAT in biological tissues [16-22] is to overcome limitations of pure optical imaging (either poor spatial resolution or shallow imaging depth) and pure ultrasonic imaging (contrast and speckle) [23].

PAT provides provide the high optical absorption contrast with good ultrasonic spatial resolution for deep imaging with the advantages of both optical and ultrasound imaging [24-31].

1.2 Fundamentals of photoacoustic imaging

Photoacoustic tomography (PAT), as an emerging technology in biomedical imaging, provides high optical absorption contrast in biological tissues. The high optical absorption contrast is derive from optical absorption in the photoacoustic excitation phase, whereas the high spatial resolution is based on ultrasonic detection in the photoacoustic emission phase. Because the ultrasonic scattering is much weaker than optical scattering and the wavelength of the photoacoustic wave is sufficiently short, photoacoustic waves provide better resolution than optical waves beyond the soft depth limit [4]. Therefore, the spatial resolution of PAT is adjustable, ranging from sub-millimeters to 15 μm, by ultrasonic detection systems with different center frequencies and detection bandwidths [32, 33]. The higher the center frequency and the wider the bandwidth, the better the spatial resolution and the shallower the imaging depth is.

In PAT, two major forms have been implemented with different types of ultrasound transducers and different image reconstruction algorithms. One is photoacoustic microscopy (PAM) and the other is photoacoustic computed tomography (PACT). The following sub-chapters will introduce them in detail.

1.2.1 Photoacoustic microscopy (PAM)

Photoacoustic microscopy (PAM) is based on a single-element focused ultrasound transducer placed confocally with the laser beam to detect PA waves traveling from focal zone. A one-dimensional (1D) image is generated by the received PA waves at each position, where the arrival time of PA wave provides the position of a source along a line, depth information. By using this time-resolved detection, axial resolution is determined,

and lateral resolution can be derived by raster scanning, acoustic focusing, or optical focusing. However, PAM usually has limitations on focal depth and imaging speed [34].

1.2.2 Photoacoustic computed tomography (PACT)

Photoacoustic computed tomography (PACT), often referred to as PAT, employs unfocused ultrasonic transducers to detect photoacoustic signals from many directions around the object for a tomographic image. It is based on the inverse algorithm [35] to reconstruct internal PA source distribution from measurements by scanning a single-element unfocused ultrasound transducer over the surface of a volume of interest [1, 36-42]. However, this scanning process can be time-consuming because it might take hundreds of scanning steps to collect PA data for an image, depending on the imaging conditions such as the size of object, transducer, and the aperture. This single-element transducer scanning usually takes several seconds, minutes or up to hours in some of the systems [43-45]. Thus, this approach is not practical for real-time clinical PA imaging requiring fast data acquisition and image reconstruction.

1.2.3 Real-time PAT

Although PAT has been considered as a novel imaging modality, use of single-element scanning has still some disadvantages such as the low imaging efficiency and instability during measurement. The transducer scan over the surface mechanically to acquire PA signals from the object. During the scanning process, the instability of the signal acquisition system causes measurement error to the image reconstruction [46-49]. In terms of imaging efficiency, fast data acquisition and PA image reconstruction algorithm are required for clinical applications. Use of the pulsed laser system with higher

repetition rate can be another approach for fast imaging [50, 51]. However, multiple excitations of a laser with higher repetition rate pulsed-laser system may damage the biological tissue of interest due to laser energy accumulation which may result in burn and inaccuracy of data. Instead of using a high repetition rate laser system, PAT can employ unfocused ultrasonic transducer arrays with a large number of elements and various designs (linear, arc, quasi, and spherical) [52-73] and inverse reconstruction algorithm to address the issue. Use of multi-element ultrasonic transducer array increases imaging speed and decrease the required number of laser excitation by using full-field illumination which can reduce the tissue injury. Real-time PAT using multi-element ultrasonic transducer array requires multi-channel data collecting system [64, 74-76] such as multi-channel parallel data acquisition (PDA), multi-channel analog-to-digital converter (ADC), multi-element graphics processing unit (GPU), and parallel computing. However, constructing such collecting systems are very complicated and expensive, so electronic multiplexing can be another approach to achieve cheap and compact system, but it increases the number of laser firing depending on the ratio of the multiplexer. It can be an issue in terms of both invasiveness and real-time imaging capability.

The spatial resolution of PAT is determined by the gap between adjacent elements, the number of transducer elements, and the bandwidth of PA signals. The gap between adjacent elements and the number of transducer elements are the key factors determining the lateral resolution. Higher lateral resolution can be achieved by reducing the gap between adjacent elements and increasing the number of elements. Axial resolution depends on the bandwidth of PA signals, and wider bandwidth yields better axial

resolution. Thus, high-resolution PA image reconstruction can be achieved by multi-element ultrasonic transducer array with high compactness and broad bandwidth. Spatial resolution is also restricted by frequency-dependent acoustic attenuation characteristics of soft tissues. Since penetration depth is also limited by acoustic and optical attenuation, spatial resolution and penetration depth can be improved with the sacrifice of each other. For deep penetration (several cm), sub-mm spatial resolution is possible, and higher spatial resolution (a few tens of μm) is possible for shallow penetration (mm) beyond one optical mean free path (~1 mm) which is the limitation of pure optical imaging. Optical absorption, in the photoacoustic excitation phase, provides dominant image contrast, which is very useful to image biological tissues with strong optical absorption characteristics.

2. FUNDAMENTALS OF ACOUSTIC DELAY LINE*

Back in old days, making RAM was very hard when computers were both analog and digital. The vacuum tube was the only way to build a memory system electronically without a transistor. One of the solutions for RAM was an acoustic delay line which used ultrasonic transducers to send a pulse through a medium and reads it out at the other ends to create a phase difference or time. Acoustic delay lines can be made of various materials such as liquid mercury [77], solid quartz crystals [78], metallic wires [79], and optical fibers [80, 81]. Based on the idea of the acoustic delay line memory, we introduced the parallel acoustic delay line (PADL) array to reduce the number of ultrasonic transducers and data acquisition (DAQ) electronics for real-time imaging. To implement multi-channel PADL array, material selection for delay line was very important. Based on the previous researches related to acoustic delay lines, we used two different materials which are optical fiber [82, 83] and silicon [84-86] among various materials.

As mentioned above, for real-time PA imaging, 1D or 2D multi-element ultrasonic transducer arrays can collect multiple PA signals in parallel without multiple laser illumination [54, 58, 87, 88] (Figure 1a). The ultrasound array can provide electronic beam forming, eliminating mechanical scanning and enabling a much faster imaging speed. Generally, the imaging speed depends on the number of transducer elements in the array.

* Part of this section is reprinted with a permission from "Parallel acoustic delay lines for photoacoustic tomography" Yapici MK, Kim C, Chang CC, Jeon M, Guo Z, Cai X, Zou J, Wang LV. 17(11):116019 [82] © 2012 by JBO and "Micromachined silicon acoustic delay lines for ultrasound applications" Chang CC, Cho Y, Wang L, Zou J. 23(2):025006 [92] © 2012 by JMM and "Handheld photoacoustic tomography probe built using optical-fiber parallel acoustic delay lines," Cho Y, Chang CC, Yu J, Jeon M, Kim C, Wang LV, Zou J. 19(8):086007 [83] © 2014 by JBO.

However, with multiple transducer elements, the construction and operation of the ultrasound receiving system become more challenging and costly. Thus, reducing or even completely eliminating the need for massive ultrasonic transducer arrays and corresponding data acquisition (DAQ) electronics is highly desirable. In our previous work, we investigated a new time-delayed ultrasound receiving concept, where each channel has different propagation length and acoustic time delay In our previous work, we investigated a new time-delayed ultrasound receiving concept based on parallel acoustic delay lines (PADLs) [82] (Figure 1b). Depending on the penetration depth (from a few mm to cm) and the speed of sound in the target tissue (~1540 m/s), the typical propagation time of a PA wave in the tissue medium is on the order of microseconds (μs). Because the repetition rate of the pulsed-laser is low, the time interval between two successively generated PA signals is on the order of milliseconds (ms) or more, which is much longer than the duration of PA signals. By introducing the specific amount of acoustic time delay (τ) to each channel, it is possible to transmit multiple channels of PA signals onto a single ultrasound transducer in one receiving cycle (Figure 1b). The acoustic time delays (t, $t + \tau$, $t + 2\tau$, $\cdots$, $t + (N-1)\tau$) are controlled by varying the propagation length of each delay line. The PA signals in multiple channels can be forced to arrive at a single-element ultrasonic transducer at different times; therefore, they are completely distinguishable in the time domain even after being mixed into a single DAQ channel. This capability opens the possibility of detecting and processing multiple time-delayed PA signals in a serial manner, using single-element transducers and single-channel DAQ electronics. As a

result, a large number of DAQ channels can be merged into one, thereby significantly reducing the complexity and cost of ultrasound receiving systems.

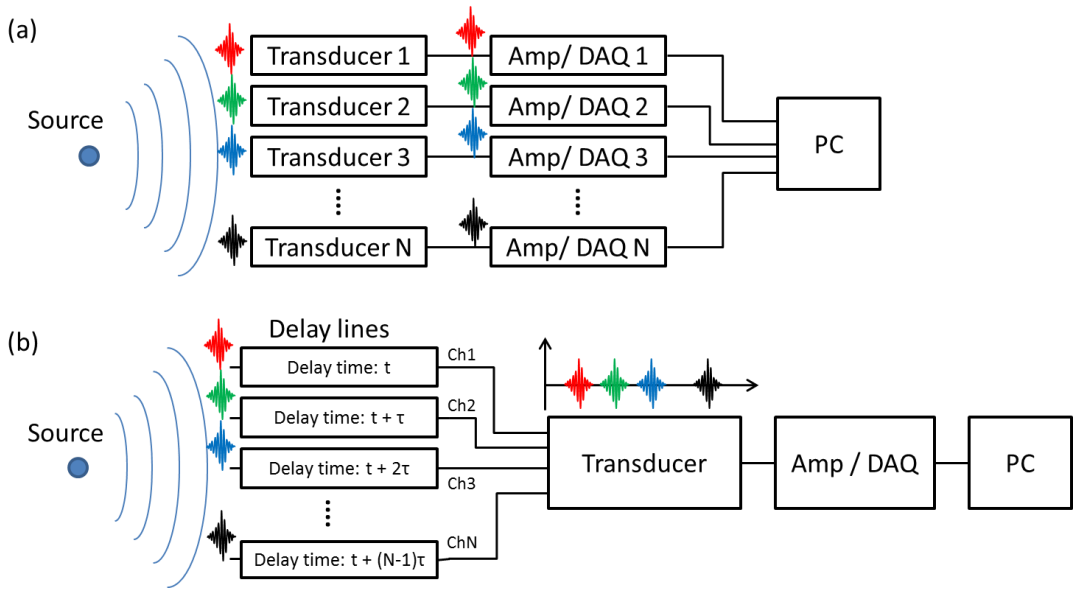

Figure 1 Concept of parallel acoustic delay line. (a) PA signal reception using multiple transducers and multi-channel DAQ electronics; and (b) PA signal reception using a single-element transducer and single-channel DAQ electronics through parallel acoustic delay lines [83]. Reprinted with permission © 2014 by JBO.

2.1 Optical fiber acoustic delay line

Optical fiber delay line has been used for various applications such as optical communication systems, phased array, and signal processing electronics requiring true time-delay phase shift. Also, optical fibers have been used to construct acoustic delay lines [80, 81]. In our previous work, Dr. Murat used low-loss fused-silica optical fibers to construct a PAT system using multi-channel PADLs.

2.1.1 Characterization method for optical fiber delay line

The acoustic properties of optical fibers were characterized to construct optical fiber PADLs. Figure 2 shows the schematic (Figure 2a) and a photograph (Figure 2b) of the experimental setup. The fibers were mounted onto a proto-board to minimize unwanted contact between the optical fiber and supporting structures. To characterize acoustic velocity in optical fiber, time delay, and acoustic attenuation, optical fibers with various lengths ranging from 10 to 35 centimeters. A generated pulse by a signal generator (1 μs width and 500 mV amplitude) was applied to the transmitting ultrasonic transducer after amplified by RF amplifier. Then, the generated ultrasound pulses transmitted through optical fibers, and detected signals were displayed and recorded by a digital oscilloscope.

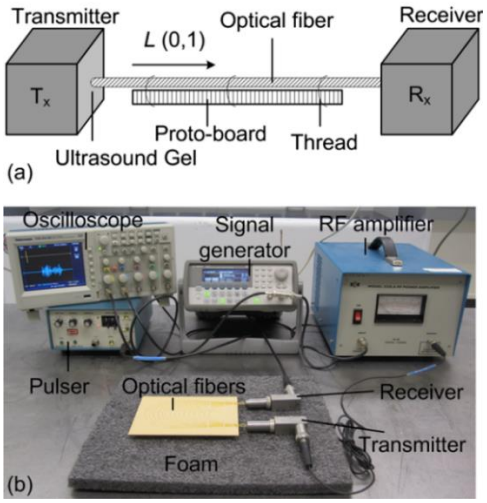

Figure 2 Acoustic characterization of optical fiber. (a) Schematic showing the arrangement of transducers with respect to the optical fiber under characterization; and (b) photograph of the entire experimental setup for acoustic characterization of optical fibers [82]. Reprinted with permission © 2012 by JBO.

2.1.2 Acoustic properties of optical fiber delay line

Figure 3a shows the ultrasonic waveforms detected from six optical fibers with different lengths ranging from 10 to 35 centimeters. The incremental time delay of ~ 10μs corresponds to propagation length difference of 5 centimeters. Figure 3b shows the acoustic time delay for each fiber. Based on the measurement, the average acoustic velocity in optical fiber was calculated as ~5108 m/s. By recording the amplitudes of ultrasonic signals detected by the receiving transducer, the average acoustic attenuation in optical fiber was calculated as ~0.2 dB/cm at 1 MHz (Figure 3c).

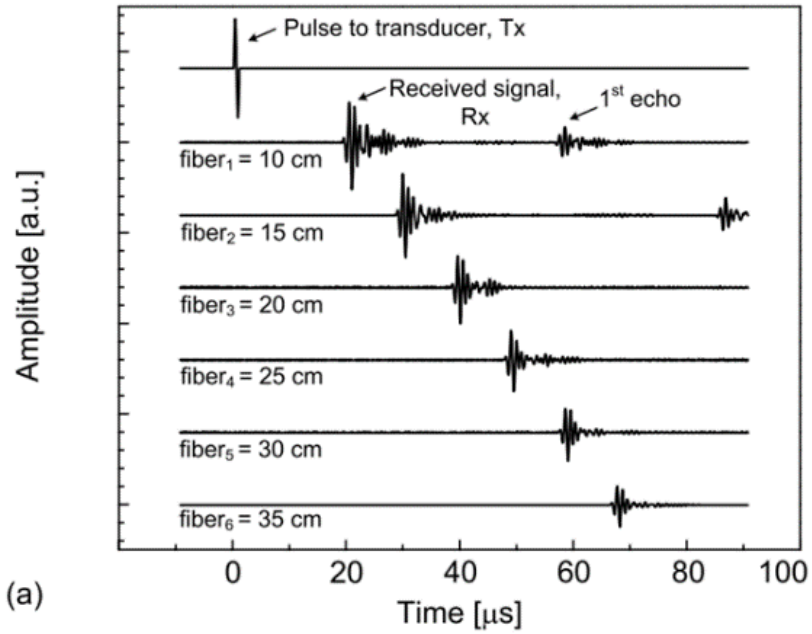

Figure 3 Acoustic properties of optical fiber delay lines. (a) Plot showing acoustic waveforms propagating through optical fibers of different lengths ranging from 10 to 35 cm. (b) Plot of the time delay versus the corresponding fiber length. The average acoustic velocity in the silica fiber is ~5108 m/s. (c) Attenuation of acoustic signals through optical fibers of various lengths. The average attenuation is ~0.2 dB/cm (0.1 dB/μs) [82]. Reprinted with permission © 2012 by JBO.

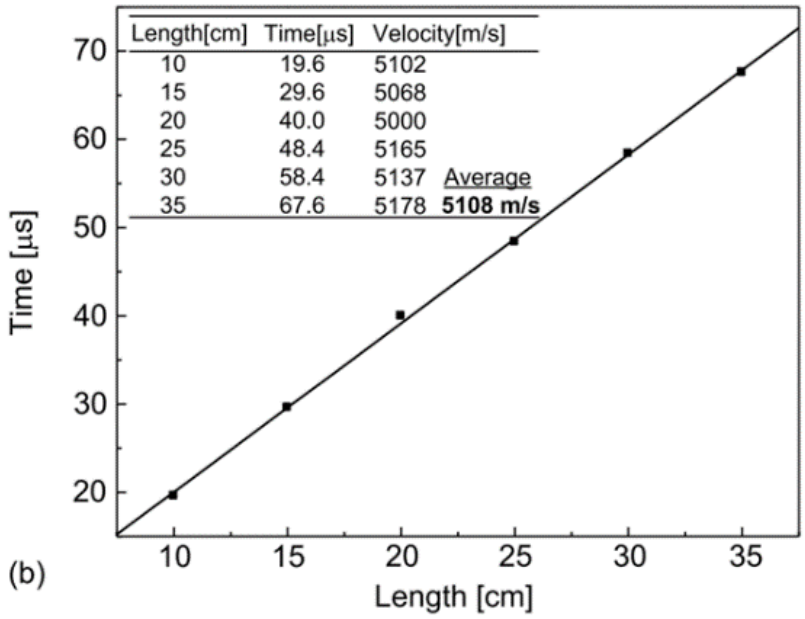

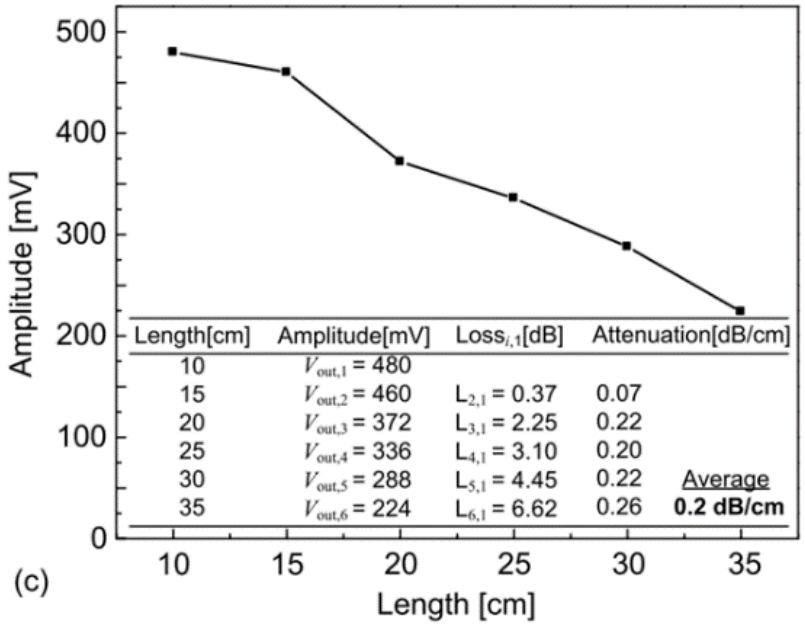

Figure 3 Continued.

2.1.3 Parallel acoustic delay line (PADL)

Based on the characterized acoustic properties optical fibers, the optical fiber PADLs were designed with following parameters: (1) the number of channels, (2) the length of each fiber, and (3) the arrangement of fibers. As the number of channels increases, the size of PADL system becomes big due to the lengths of optical fibers. First, to achieve a compact design of PADL, the number of channels was selected as 8. Second, to determine the length of each fiber, we considered two important design criteria as the following: (1) incremental time delay between each fiber to avoid signal overlapping, and (2) proper fiber lengths to prevent interferences between echo signals and original signals. To satisfy both, the length of shortest optical fiber was designed into 225 mm (i.e. acoustic time delay of 44 μs), and the incremental time was designed into 12 μs. Table 1 shows the time delays for the 8-channel optical fiber PADL with the corresponding fiber lengths.

Table 1 Time delays for the 8-channel PADL with the corresponding fiber lengths [82]. Reprinted with permission © 2012 by JBO.

Fiber number	Signal arrival (μs)	1st Echo arrival (μs)	Fiber length (mm)
1	44	132	225
2	56	168	286
3	68	204	347
4	80	240	409
5	92	276	470
6	104	312	531
7	116	348	593
8	128	384	654

For the arrangement of optical fiber PADL, Lucite (acrylic) housing with ~200-μm-wide trenches was fabricated (Figure 4a). Ends of optical fibers were polished for good acoustic coupling (Figure 4b). A total of sixteen optical fibers are composed of two channels of eight PADLs. All 16 fibers are connected to an input port for PA signal transmission, and each channel of 8 fibers is connected to each output port (receiving ultrasonic transducer) for PA signal detection (Figure 4c).

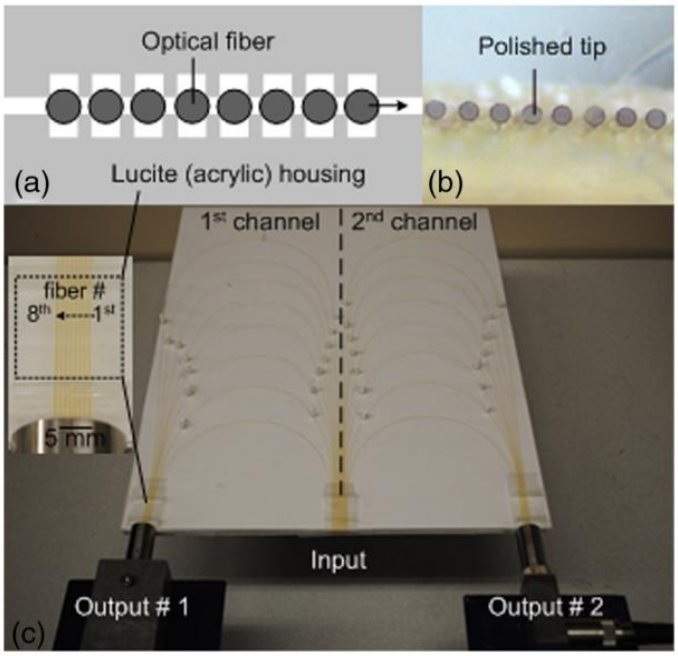

Figure 4 16-channel optical fiber parallel acoustic delay line. (a) Schematic of the parallel arrangement of fiber endings in equally spaced trenches. (b) Optical microscopic image showing polished tips of fibers. (c) Picture of the PADL array having a common input and two output channels. Inset shows the picture of equally spaced Lucite grooves housing the fiber endings [82]. Reprinted with permission © 2012 by JBO.

In this research, to provide proper acoustic time delays (e.g., 12 μs) that will avoid possible mixing of multiple PA signals, each two adjacent PADLs had to differ in length

by around 6 cm. As a result, the lengths of the PADLs increased dramatically with the number of the PADLs. For example, the longest delay line in an 8-PADL array was more than 65 cm. Further, to avoid excessive acoustic attenuation, distortion, cross-talk, and potential mechanical fracture of the fused-silica fibers, the PADLs were laid out across a large area. However, this situation not only limited the total number of PADLs that could be practically constructed but also impeded the use of the PADL technique in real biomedical applications.

2.2 Micromachined silicon acoustic delay line

Optical fiber PADL shows good performance such for real-time PAT with a channel reduction ratio of 8 to 1. However, as the number of channels of PADL increases, the optical fiber delay line needs to be very long for sufficient acoustic time delay due to the high acoustic velocity in the optical fiber (~5108 m/s) [82]. Moreover, it is hard to make optical fiber compact because small bending radius can cause breakage of optical fibers due to its stiffness. These disadvantages limit the possibility of channel expansion which can improve the imaging speed of PAT. To address this issue in our previous research, we developed a new micromachined silicon acoustic delay lines with more compact design and better acoustic properties.

2.2.1 Design of silicon acoustic delay line

Silicon has extremely low acoustic attenuation in the MHz ($\sim 10^{-4}$ dB mm^{-1} MHz^{-2} @ 10 MHz) [89], and excellent thermal stability. Multiple delay lines can be fabricated with microfabrication process. The dimension of the silicon delay line is related to the acoustic transmission. To suppress high order mode signals, the dimension of a silicon

delay line should satisfy (df/V_0) << 1, where d is the width or thickness of the silicon delay line (whichever is smaller), f is the frequency of the PA signal, and V_0 is the acoustic velocity in delay line [90]. Based on the inequality mentioned above, the dimension for delay line should be much smaller than 3.7 mm for a 2.25 MHz center frequency since the acoustic velocity in silicon is ~8430 m/s [91]. To satisfy the condition, all the silicon delay line was designed to have a width of 500 μm and a thickness of 250 μm. To characterize the acoustic properties of silicon, delay line structures were designed into different shapes.

2.2.2 Fabrication of delay line structure

For fabrication of silicon delay line structure, first, the 300 nm-thick aluminum layer was deposited on the 250 μm thick 4-inch silicon wafer using e-beam evaporation. The aluminum layer was patterned using photolithography. As the last step, a cryogenic deep reactive ion etching (DRIE) process was conducted to etch the silicon delay line structures. For DRIE process, the silicon wafer was fixed on a dummy wafer with Fomblin oil (Fomblin 06/6, Solvay Plastics, Brussels, Belgium). To completely etch through 250 μm thick silicon wafer, 60 min DRIE was conducted at a temperature of -120°C cooled down by using liquid nitrogen. For anisotropic etching with better sidewall profile, helium backing between dummy wafer and the chuck was conducted. The etched silicon delay lines were carefully removed from the silicon wafer.

2.2.3 Characterization setup

Figure 5 shows the characterization setup. Acrylic holding structures were used to support the silicon delay lines for minimal signal leakage. The delay line and ultrasound transducer are fixed on the translation stage. Nd: YAG laser (Quanta-Ray Pro-200,

Newport Corporation, Irvine, CA, USA) with a 1064 nm wavelength, a 10 Hz repetition rate, and 10 ns pulse width, was used to directly generate acoustic wave signal in silicon through the photoacoustic effect [92]. The laser propagated through a half-wavelength wave plate for attenuation, a dielectric polarizer, two filters, and an objective lens for focusing. The acoustic wave is detected by an ultrasound transducer with a 2.25 MHz center frequency (V105, Olympus NDT, Waltham, MA, USA). The received signal is amplified by the pulser–receiver unit (5072-PR, Olympus NDT, Waltham, MA, USA) and displayed on an oscilloscope.

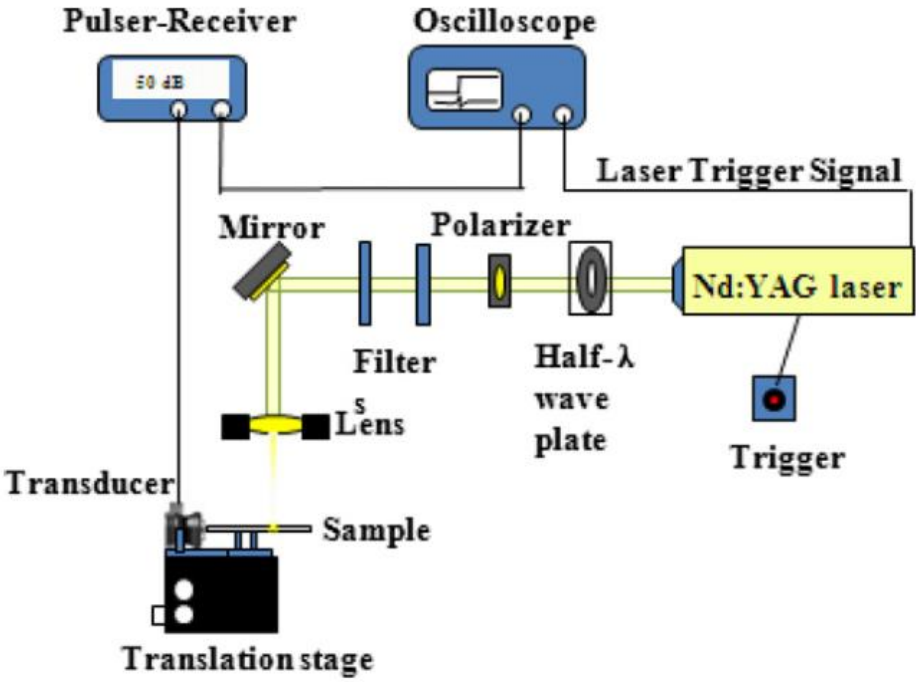

Figure 5 Schematic of the photoacoustic excitation setup [93]. Reprinted with permission © 2013 by JMM.

2.2.4 Acoustic properties

A straight silicon delay line was used to calculate the acoustic attenuation and velocity (Figure 6a). To measure the acoustic velocity and attenuation in silicon, the laser was focused on the delay line at eight different points with ~5 mm intervals (Figure 6b). The acoustic waves, generated by photoacoustic effect, were received by the ultrasound transducer. The average velocity was calculated as ~8454 m/s (Figure 6c). The attenuation was calculated by measuring the amplitude change of the signal. There was no significant change in amplitude for both the simulation (Figure 6d) and experimental results (Figure 6e), so the acoustic attenuation in a silicon delay line is extremely low.

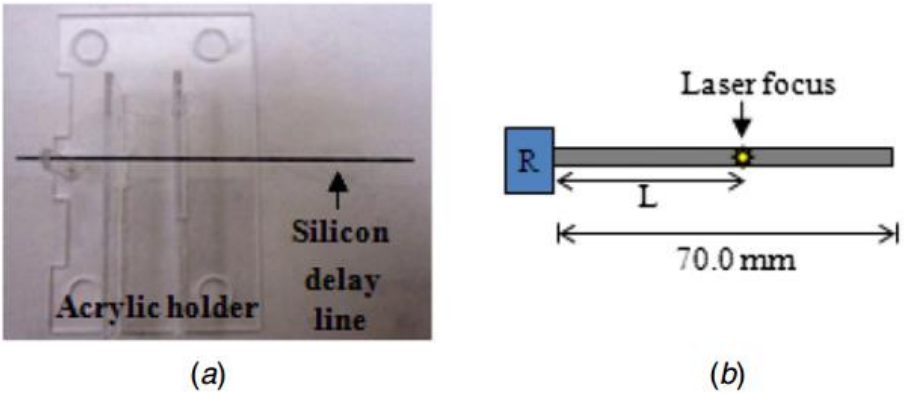

Figure 6 Straight silicon delay-line measurements. (a) sample; (b) measurement setup: receive signal from focus points along the straight delay line. L: traveling length (distance from the focal point to the transducer). R: receiving transducer; (c) plot of the arrival time versus traveling length. The average velocity in straight silicon delay line is ~8454 m/s. Inset: representative signal shape from L: 28.2 mm; (d) simulation results of signal peak–peak amplitude versus traveling length. Inset: representative signal shape from L: 30 mm; and (e) experimental results of signal peak–peak amplitude versus traveling length. Inset: representative signal shape from L: 28.2 mm [93]. Reprinted with permission © 2013 by JMM.

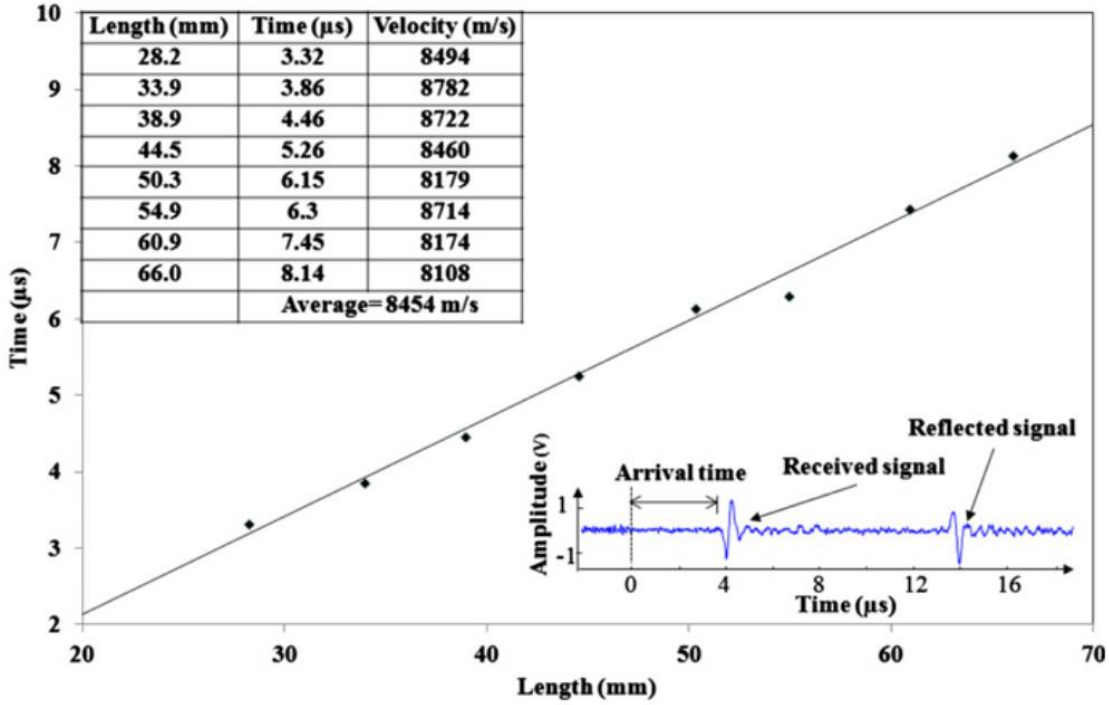

(*c*)

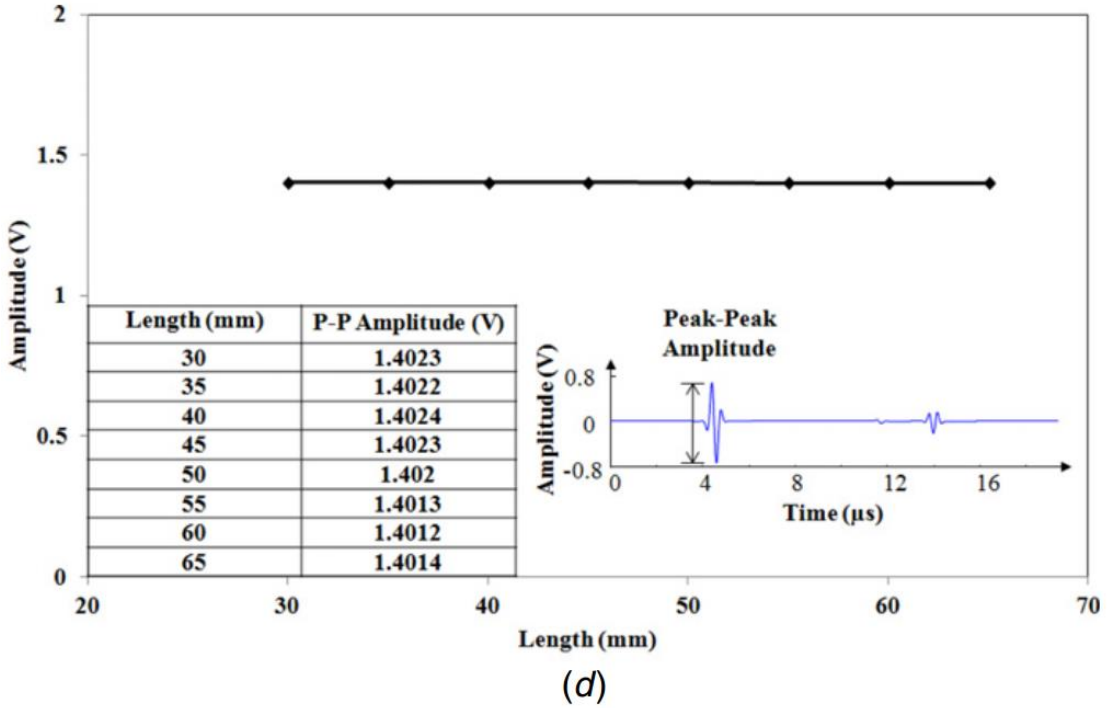

(*d*)

Figure 6 Continued.

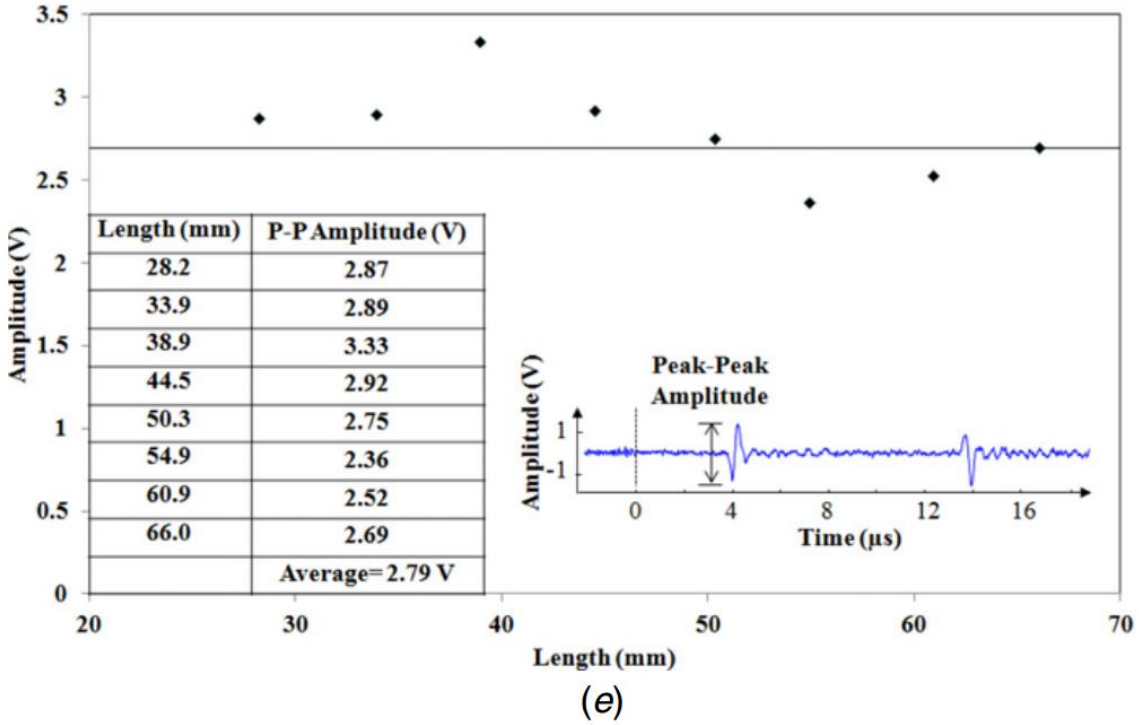

(*e*)

Figure 6 Continued.

2.2.5 Propagation in U-turn structures with different bending radii of curvature

As shown in Figure 7a, U-turn structures with six different bending radii of curvature were experimented to investigate the effect of the circular shape on the acoustic transmission. The laser excitation was conducted on the two points (i.e. points A and B in Figure 7b), respectively to see the signal difference depending on the curvature. Since the acoustic attenuation in silicon is very low at 2.25 MHz, curved portion is main reason to cause difference between two signals. The simulation (Figure 7c) and experimental results (Figure 7d) show that amplitude ratio decrease as the bending radius of curvature decreases. The signal reduction is mainly due to the mode conversion and direct reflection of the waves. The experiment results with U-turn structure shows that minimum radius of

curvature must be larger than 2 mm to transmit acoustic signals for high transmission efficiency.

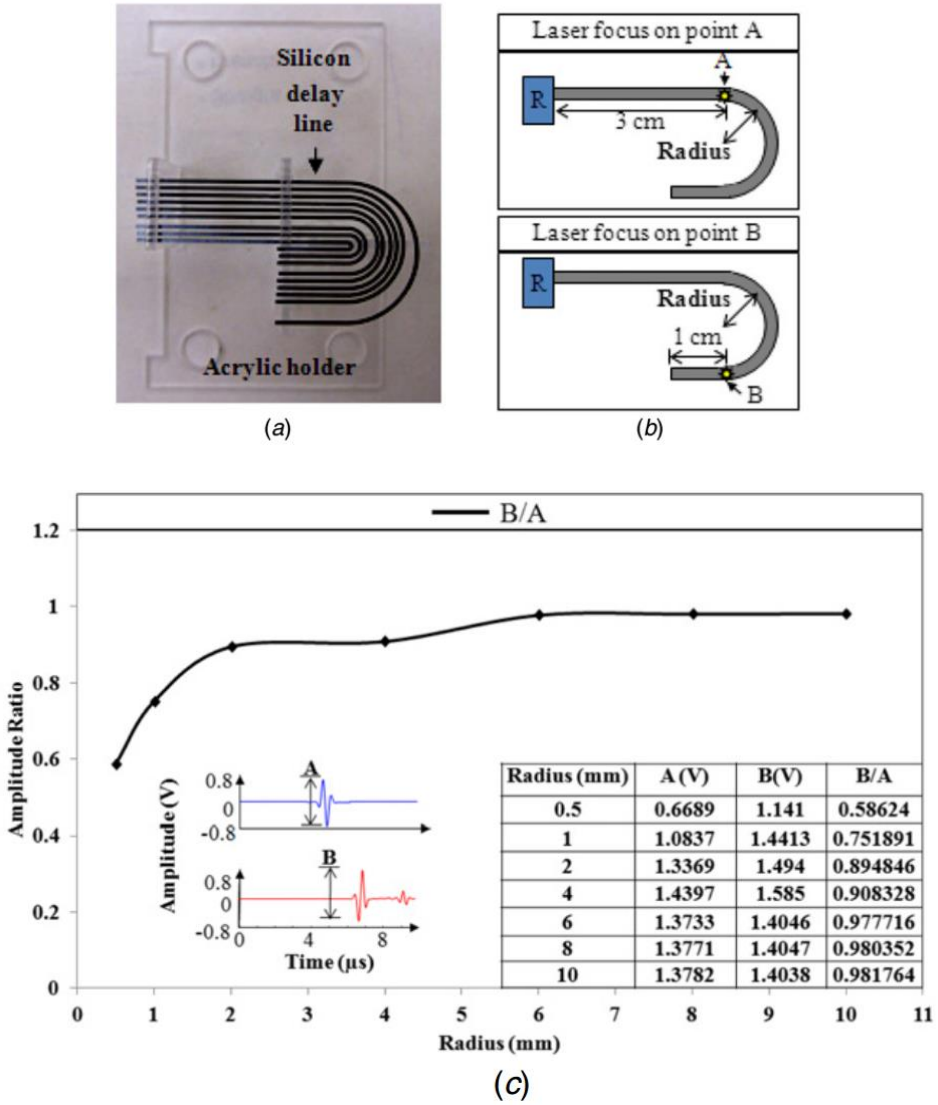

Figure 7 U-turn structure measurements. (a) sample; (b) measurement setup: receive signals from different focus points, A: without bending, B: with bending; (c) simulation results of radius versus amplitude ratio. Inset: representative signal shape from turns with 6 mm radius; and (d) experimental result of radius versus amplitude ratio. Inset: representative signal shape from turns with 6 mm radius [93]. Reprinted with permission © 2013 by JMM.

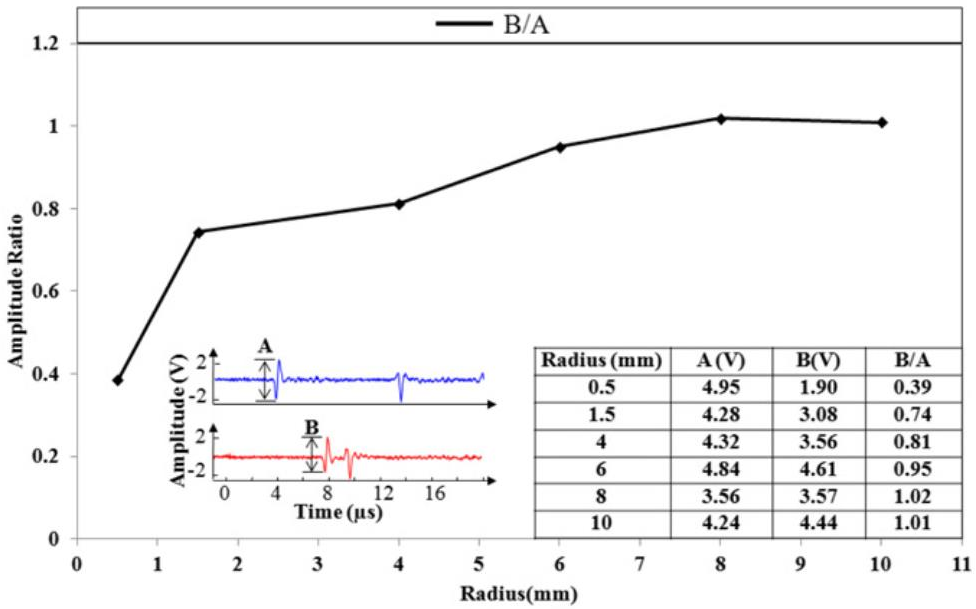

Radius (mm)	A (V)	B(V)	B/A
0.5	4.95	1.90	0.39
1.5	4.28	3.08	0.74
4	4.32	3.56	0.81
6	4.84	4.61	0.95
8	3.56	3.57	1.02
10	4.24	4.44	1.01

(*d*)

Figure 7 Continued.

2.3 Summary of work

In section 3, the design, fabrication and testing of a multi-channel optical fiber parallel acoustic delay line array for hand-held photoacoustic tomography is presented [83]. Its compact size by using laser-micromachined acrylic spacer structures and threaded optical fiber acoustic delay lines open the possibility of hand-held PAT operation with a channel reduction ratio of 8:1. Laser-micromachined acrylic spacers consist of a number of elliptical holes for threading optical fibers and L-shaped isolation trenches to minimized signal crosstalk between adjacent fibers. This PADL array has been used to conduct photoacoustic imaging with optical imaging phantom. Based on the imaging result, the reconstructed PA image matches well with the actual phantom, so its PA imaging capability has been demonstrated successfully.

In section 4, the design, fabrication, acoustic simulation, and testing of multi-channel silicon PADL probe for real-time PAT is discussed [84]. Single-crystalline silicon has been used to construct PADLs instead of optical fiber which was used in the previous research. Each silicon acoustic delay line is designed into spiral coil pattern to minimize the size of the delay line. The distance between input and output is fixed in all delay lines for the alignment. Since fabricated silicon delay line is very fragile, acrylic housing structure was fabricated by the laser-micromachining process to securely protect silicon PADLs from external forces. 16-channel silicon PADLs has been evenly spaced by specially designed micro-spacer structures which consist of sixteen delay line trenches and fifteen isolation trenches to minimize signal crosstalk. As done with optical fiber PADLs, PA imaging experiment was conducted. Silicon PADL array also shows good performance for photoacoustic imaging from the experiment result.

In section 5, the design, structural simulation, acoustic simulation of linker structures for structural stability of silicon acoustic delay lines and acoustic simulation of tapered input terminal design for better elevational spatial resolution were discussed [86]. To securely support long silicon acoustic delay line without severe deformation, linker structure was designed and simulated. The structural simulation was conducted to show the usefulness of linkers and acoustic simulation was conducted to find proper material for it. 3D-printed micro linker structure was designed and printed directly by a high-resolution 3D-printer. Ultrasonic transmission testing was conducted with a silicon acoustic delay line and 3D-printed linker structure assembly. For better spatial resolution, tapered input terminal design was introduced and simulated.

3. MULTI-CHANNEL OPTICAL FIBER PARALLEL ACOUSTIC DELAY LINE (PADL) ARRAY FOR HANDHELD PHOTOACOUSTIC TOMOGRAPHY PROBE[*]

For hand-held PAT operations, a miniaturized PADL probe was developed. The PADL probe consists of 16 PADLs (made of fused-silica optical fibers) arranged into two bundles, which allows the simultaneous collection of 16 channels of the PA signals in one illumination-receiving cycle, using just two single-element transducers and two channels of DAQ electronics. To minimize the size of the PADL probe, all the PADLs are tightly wound into a spiral pattern with a suitable radius of curvature to avoid excessive acoustic attenuation and distortion. To provide robust support for all the delay line structures, plastic spacers with specially designed isolation trenches were fabricated using laser micromachining. The ultrasonic transmission properties of the individual PADLs were characterized and verified using two-port ultrasound measurements. To test its photoacoustic imaging capability, we used the assembled PADL probe to collect photoacoustic signals from a black-ink target embedded in an optical phantom tissue.

3.1 Design of the 16-channel optical fiber PADL array probe

As shown in Figure 8, the 16-channel handheld PADL probe consists of one input port, two output ports, and a PADL housing unit located between. At the input port, all of the 16 PADLs receive incoming PA signals. After routing through the PADL housing unit, the 16 PADLs are divided into two arrays, each of which goes to one output port.

[*] Part of this section is reprinted with a permission from "Handheld photoacoustic tomography probe built using optical-fiber parallel acoustic delay lines," Cho Y, Chang CC, Yu J, Jeon M, Kim C, Wang LV, Zou J. 19(8):086007 [83] © 2014 by JBO.

Compared with bundling all 16 PADLs together, the 2-by-8 design reduces the total length of the PADLs and allows a much more compact probe structure, while requiring only one additional ultrasonic transducer and DAQ system.

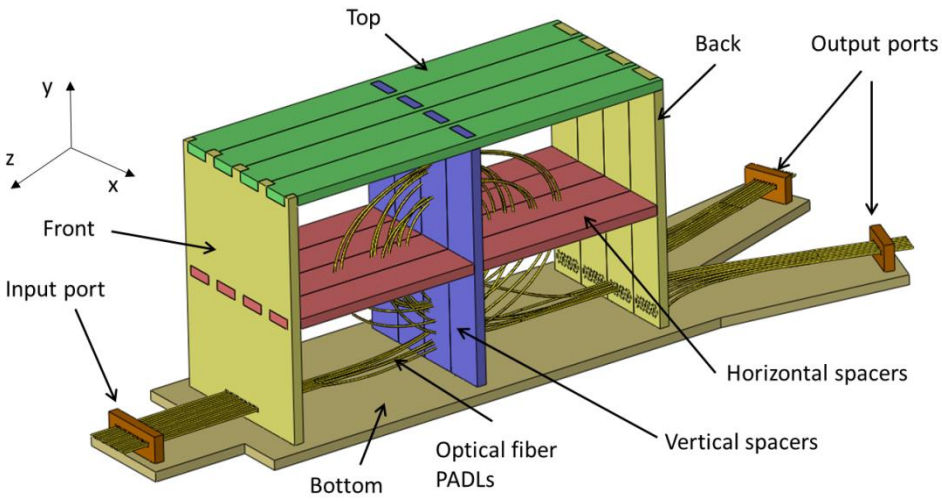

Figure 8 Schematic of the 16-channel handheld PADL probe: a perspective view of the probe input port, the PADL housing unit, and two output ports [83]. Reprinted with permission © 2014 by JBO.

3.2 Probe design and construction

3.2.1 PADL fabrication

Building on Murat's previous results [82], the PADLs were designed to provide good mechanical stability and acoustic performance. Due to their broad availability, low cost, and low acoustic attenuation at ultrasonic frequencies (i.e., MHz), fused-silica optical fibers (CeramOptec Inc., MA) with a total diameter of ~220 μm were used in the PADLs. In a cylindrical wire-type ultrasound delay line, the acoustic delays can vary with different

frequencies. To transmit desirable ultrasound signals in the wire-type delay lines, the second and higher-orders of longitudinal mode and mode dispersion should be suppressed by satisfying the following condition [94, 95]

$$\frac{df}{V_O} \ll 1, \qquad \text{(Equation 1)}$$

where d is the diameter of the optical fiber, f is the frequency of the ultrasonic waves, and V_O is the acoustic velocity in the optical fiber. At a center frequency of 2.25 MHz, the small diameter of the optical fiber and the high acoustic velocity (5000~6000 m/s) of fused silica allow good suppression of both higher-order modes and mode dispersion to ensure clean transmission of PA signals. Based on the acoustic properties of the optical fibers, we kept the following design specifications in mind: (1) the time delay of the shortest PADL, (2) the time delay increment needed to prevent overlapping, and (3) the parallel arrangement of fibers and pitch between fibers at the input port.

The acoustic time delays were controlled by varying the length of the delay lines, determined by the following two criteria [82]. First, the time delay between each delay line had to be long enough to prevent signal interference from neighboring delay lines. In our PADLs, the length differences between two adjacent delay lines were determined to be 5.00 cm long, which corresponded to an incremental time delay of 10 μs. Since the time duration of the PA signal from each delay line is less than 6 μs, a 10 μs delay is adequate. Second, the PA signal in the longest (8th) delay line had to reach the receiving transducers before the 1st reflected signal (1st echo, a signal reflected twice by the two

ends of the optical fiber) in the shortest delay line, to avoid possible interference between them. Representing the time delay of the 1st delay line as T_1 (in μs), the 8th signal will reach the receiving transducer after T_1+70 μs, and the 1st echo will be detected at $3T_1$. To avoid interference, an inequality of $3T_1 > T_1$+70 is required, and therefore T_1 should be greater than 35 μs. Based on this calculation, the time delays of the shortest (1st) delay line and longest (8th) delay line were designed for 40 and 110 μs, respectively. The time delays and delay lengths for the 8-channel PADL array are summarized in Table 2. In common ultrasonic array systems, the transducer elements are arranged with $p < \lambda/2$, where is the pitch and λ is the ultrasound wavelength. Based on the ultrasound frequency (2.25 MHz) of our ultrasonic transducers, the pitches between two adjacent fibers were determined to be 500 μm. Since the optical fibers have an overall diameter of 220 μm, a fiber-to-fiber spacing of 300 μm was chosen for arranging the PADLs at the input port.

Table 2 Time delays and optical fiber lengths for the 8-channel PADL array [83]. Reprinted with permission © 2014 by JBO.

Fiber Number	Time Delay (μs)	Optical Fiber Length (cm)
1	40	21
2	50	26
3	60	31
4	70	36
5	80	41
6	90	46
7	100	51
8	110	56

3.2.2 Fiber spacer structure design and fabrication

To securely position the optical-fiber PADLs, four pairs of spacer structures were designed and fabricated (Figure 9a), each having a horizontal and a vertical member assembled into a cross. On each spacer structure, there is a two-dimensional matrix of elliptical holes (800 μm long and 300 μm wide) for assembling the optical fibers. Unlike circular holes, the elliptic holes can provide relief clearance in the direction of optical fiber bending, which helps to reduce the chance of breaking the optical fibers during threading. To reduce possible acoustic coupling between two adjacent optical fibers passing through the spacer structure, an "L" shaped isolation trench was cut around each elliptic hole, as seen in Figure 9b. The length and width of the isolation trenches were 2.15 mm and 250 μm, respectively. To accommodate even the longest optical fiber (~56 cm), the horizontal spacer structure has an array of 4-by-30 elliptic holes and the vertical spacer structure has an array of 4-by-18 elliptic holes. Overall, the spacer structures measure 6.2 mm by 60 mm horizontally (x-z) and 6.2 mm by 35.5 mm vertically (x-y). These dimensions allow the longest fiber to be snugly wound with the smallest radius of curvature of around 5 mm without breaking.

When a sound wave is an incident at an oblique angle onto an interface of two materials with different acoustic impedances, one form of vibrational motion (e.g., longitudinal) can be transformed into another one (e.g., transverse). This phenomenon is called (acoustic) mode conversion. The mode conversion could occur at the bent section of an optical-fiber PADL, depending on the both the wavelength of the PA signals and the

bending radius. Generally, a larger bending radius creates less mode conversion. In PA imaging, the PA signals are launched and received in the longitudinal mode. Therefore, any conversion to other modes during their transmission in the optical-fiber PADLs should be avoided. Based on our previous studies [82], a smallest bending radius of 5 mm was maintained in winding the optical fiber PADLs to minimize the mode conversion.

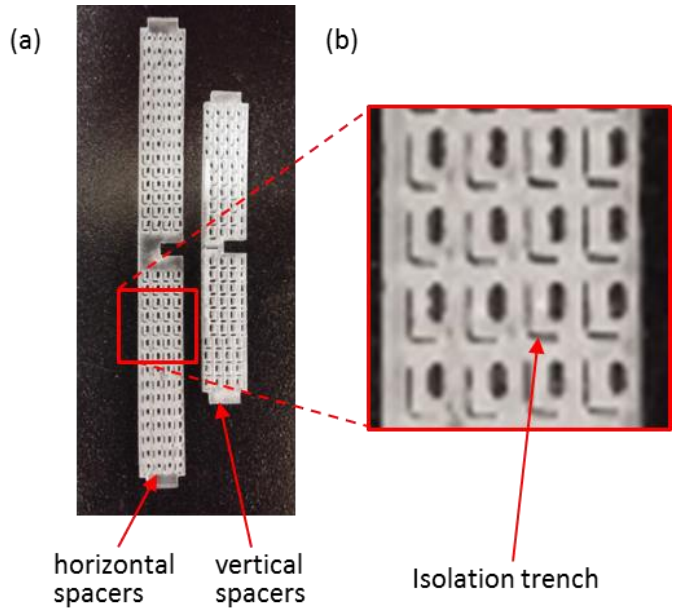

Figure 9 Fiber spacer structures. (a) Horizontal and vertical spacers fabricated using laser micromachining; and (b) Zoom-in view of the horizontal spacer showing the elliptical threading holes and "L" shaped isolation trenches [83]. Reprinted with permission © 2014 by JBO.

3.2.3 Probe construction

The first step to construct the hand-held PADL probe was preparing the optical-fiber PADLs. 16 optical fibers were cut to their requisite lengths, and both ends of each

optical fiber were polished. Then a laser micromachining system (Universal Laser Systems, PLS6.75) was used to cut the input/output fiber holders, the top, bottom, front, and back plates of PADL housing unit, and four pairs of optical fiber spacers from a 1.5-mm-thick acrylic sheet. To assemble the PADL probe, the input and output holders for fiber arrangement were first fixed on the bottom plate. Second, the front and back panels were fixed on the bottom plate. Third, the horizontal and vertical spacers were assembled crosswise. The main housing part, including the front/back panels and crossed horizontal/vertical spacers, was fixed on the bottom plate. The last step was carefully threading the optical probe fibers through the input port, front panel, vertical/horizontal spacers, back panel, and the output port. Since the coiled optical fibers are flexible springs under compression, the lengths of the input and output port were carefully adjusted to provide the best contact condition. The fully assembled PADL probe is shown in Figure 10.

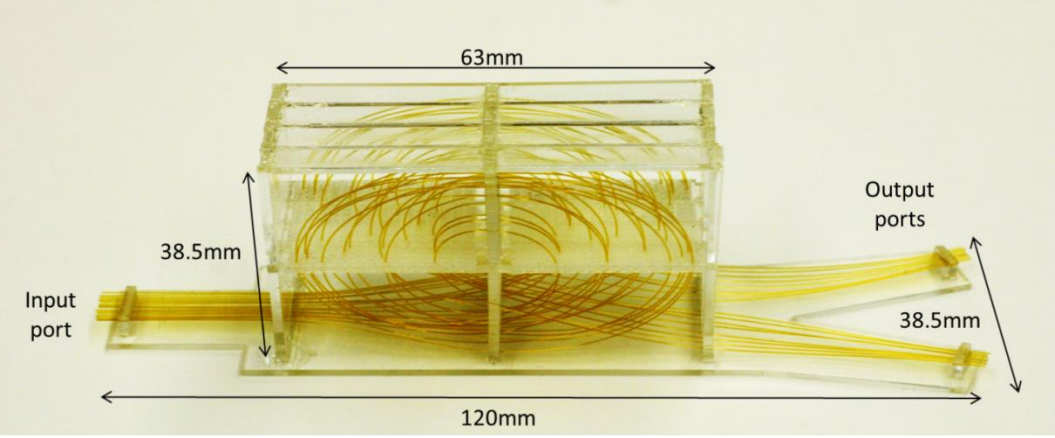

Figure 10 Fully assembled optical fiber PADL probe [83]. Reprinted with permission © 2014 by JBO.

3.3. Ultrasonic characterization and PAT imaging

3.3.1 Ultrasonic testing setup

We set up a simple experimental system to characterize the ultrasonic transmission properties of the 16-channel PADLs. The pulser/receiver (Olympus NDT, 5072PR) was set to transmission mode. Three ultrasonic transducers (Olympus NDT, V106-RB, 2.25 MHz) were used in the testing, with one serving as the transmitter and the other two serving as the receiver. The transmitting transducer was interfaced with the input port of the 16-channel PADLs. The two receiving transducers were interfaced with the two output ports of the PADLs, respectively. To enhance coupling efficiency and minimize unwanted reverberation, mineral oil was applied to the surfaces of the transducers and the ends of the PADLs. The ultrasound signals (generated by the transmitting transducer) traveled from the input port to the two output ports through the 16-channel PADLs with different time delays. Since the pulser/receiver had only one receiving port, the two receiving transducers were connected to the pulser/receiver one at a time to receive all ultrasound signals from the 16 optical fibers, which were averaged 16 times to improve the signal-to-noise ratio (SNR), displayed, and recorded on the digital oscilloscope (Tektronix, TDS2014B).

3.3.2 PAT imaging setup

The experimental setup of the PA imaging experiment is shown in Figure 11. The light source was a frequency-doubled Q-switched Nd:YAG laser (Continuum, SL2-10) with a pulse duration of 5 ns, a pulse repetition rate of 10 Hz, and a wavelength of 532 nm. After it passed through several prisms, the light beam was focused on a phantom via

a cylindrical lens, parallel to the alignment of the delay lines. The laser pulse energy was less than 10 mJ/cm^2, much lower than the ANSI safety limit (20 mJ/cm^2 at 532 nm).

The induced PA waves propagated from the phantom and traveled along the PADLs into two DAQ channels. In each DAQ channel, 8 time-delayed PA signals were sequentially detected by a single-element unfocused ultrasonic transducer (Olympus NDT, V303). The delivered PA signals were amplified by an ultrasound pulser/receiver (Olympus NDT, 5072PR). An oscilloscope (Tektronix, TDS5054) recorded these signals at a sampling rate of 5 MHz.

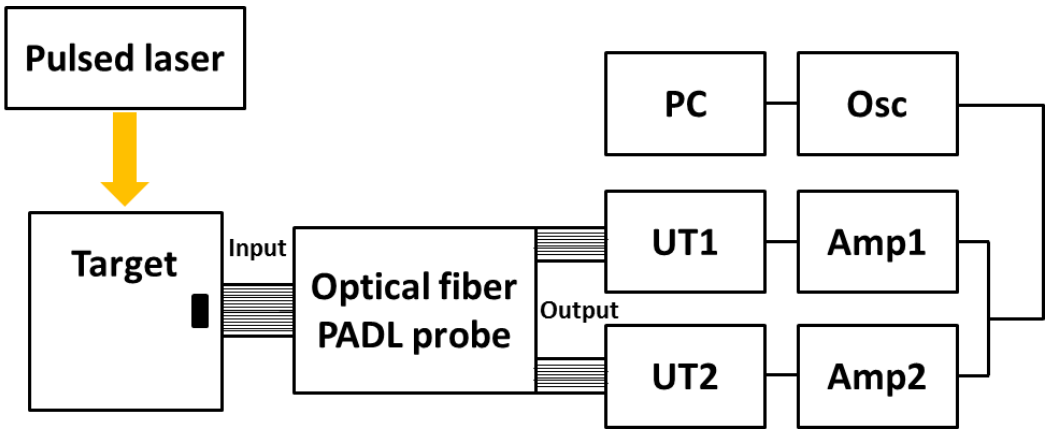

Figure 11 PAT imaging setup using the 16-channel PADL probe [83]. Reprinted with permission © 2014 by JBO.

3.3.3 Data acquisition and image reconstruction

The PA signals were averaged 10 times to generate one PA image. Thus, the imaging speed was 1 Hz. The end of each delay line on the sample surface was considered as a single ultrasound element in an ultrasound array system. Each PA signal sequentially

detected by one DAQ channel was reshaped into eight separate PA signals, based on the predefined time positions, measured by the ultrasound transmission experiment. The differences in acoustic attenuation in each fiber were compensated for (0.2 dB/cm). Then, a commonly used delay-and-sum image reconstruction method was applied to reconstruct the PA images [35]. Briefly, the PA images were reconstructed by summing the data from all channels after compensating for time delays at each fiber, based on its length and matching phase. In a two-dimensional beam field along the x and z directions, a time delay τ_n for the n^{th} PADL located on (x_n, z_n) can be calculated as follows:

$$t_n = \frac{\sqrt{(x - x_n)^2 + (z - z_n)^2} - R}{c} \qquad \text{(Equation 2)}$$

where R is the distance from a focusing point to the center of the delay line and c is the speed of sound in soft tissues, 1540 m/s. Envelope detection was applied by using Hilbert transformation along the axial direction (i.e., the z direction) followed by taking the absolute value.

3.4 Result and discussion

3.4.1 Ultrasonic transmission through the PADLs

Figure 12a shows the 8 channels of time-delayed ultrasound signals followed by the 1st channel's echo signal received by ultrasonic transducer UT1, and Figure 12b shows a zoom-in view of the first three ultrasound signals. Similarly, Figure 12c shows the 8 channels of time-delayed ultrasound signals followed by the 1st channel's echo signal received by ultrasonic transducer UT2, and Figure 12d shows a zoom-in view of the first

three ultrasound signals. Ultrasound signals naturally attenuated along the length of the PADLs. Theoretically, acoustic attenuation should be exponential to the delay length by Beer's Law. However, the observed nonlinear attenuation of the PADLs could be caused by non-uniform contacts between the PADLs and the transducers. The average attenuation was calculated to be 0.19 dB/cm at 2.25 MHz by measuring the signal amplitude difference between the shortest fiber and the longest one. This value is similar to that observed before (0.2 dB/cm at 1 MHz) [82]. Figures 12b and 12d show incremental time delays of ~9.5 μs.

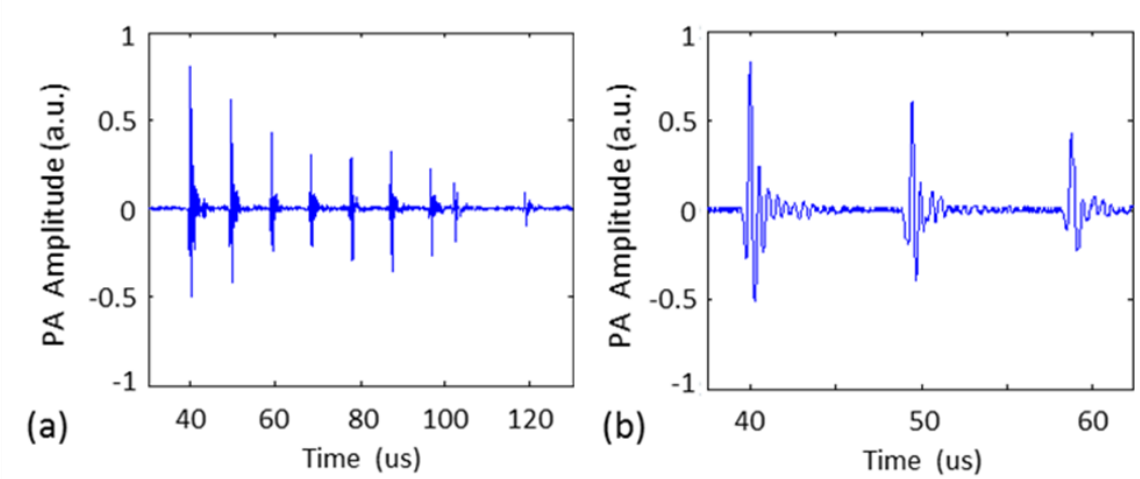

Figure 12 Plots of acoustic waveforms propagating through the optical-fiber PADLs with various lengths ranging from 21 cm to 56 cm: (a) Raw A-line signals obtained by ultrasonic transducer UT1; (b) Zoom-in view of the first three signals in (a); (c) Raw A-line image obtained by ultrasonic transducer UT2; and (d) Zoom-in view of the first three signals in (c) [83]. Reprinted with permission © 2014 by JBO.

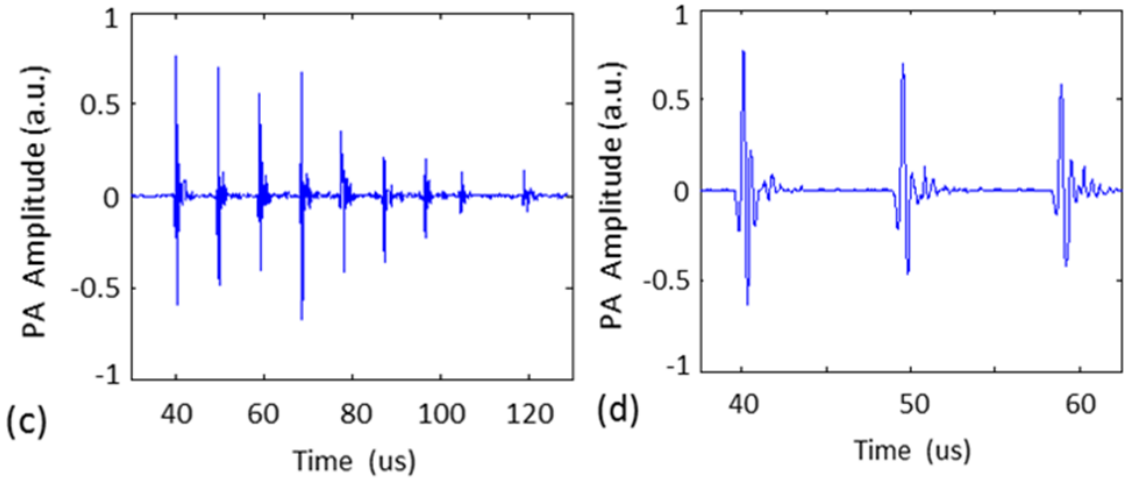

Figure 12 Continued.

3.4.2 PAT Imaging

To demonstrate the PA imaging capability of the handheld PADL-PAT probe, we imaged an optically absorptive target (2.5 mm × 1 mm × 2.5 mm along the X, Y, and Z axes, respectively) embedded in an optically scattering tissue phantom (100 mm × 100 mm × 50 mm along the X, Y, and Z axes, respectively), shown in Figure 13a. The phantom consisted of 10% gelatin by weight and 1% intra-lipid by volume, and its reduced scattering coefficient was ~9 cm^{-1}. The object was located 2.5 mm below the phantom's surface. The optical absorption coefficient of the target was ~100 cm^{-1}. The raw A-line data with Hilbert transformation acquired by both channels are shown in Figures 13b and 13c.

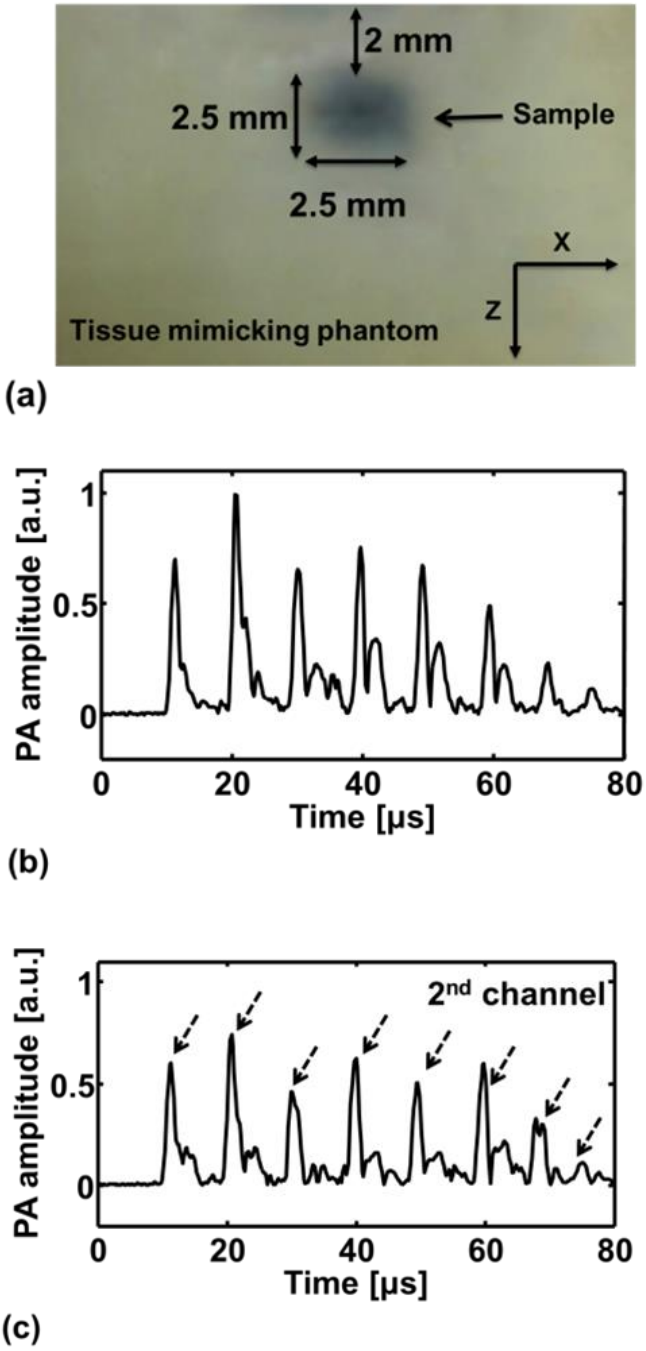

Figure 13 PA imaging phantom and raw PA signals. (a) Photograph of an optically absorbing target embedded in an optically scattering medium; (b) Raw A-line PA signals with Hilbert transformation obtained by the ultrasonic transducer (UT 1); and (c) Raw A-line PA signals with Hilbert transformation obtained by the ultrasonic transducer (UT 2) [83]. Reprinted with permission © 2014 by JBO.

The A-line PA data from both channels were rearranged into one raw Hilbert-transformed PA B-scan image, shown in Figure 14a. The reconstructed PA images are presented with compensation for the ultrasound attenuation (0.2 dB/cm) in each fiber, as shown in Figure 14b. The reconstructed PA images match well with the photograph in Figure 14a. The image contrast, defined as $(PA_{target} - PA_{background})/PA_{background}$, is calculated to be ~ 2.4. The spatial resolution, defined as the one-way distance between 10% and 90% of the maximum over the minimum, is ~1.1 mm. Compared to our previous results [82], we found that the PA signals were broadened and noisier due to the increased contact junctions and bends of the optical fibers in the small housing unit. Thus, the image contrast and spatial resolution were slightly diminished, by 20 and 37%, respectively. Further, the enhanced PA image can be presented after the signal threshold of 30% (Figure 14c).

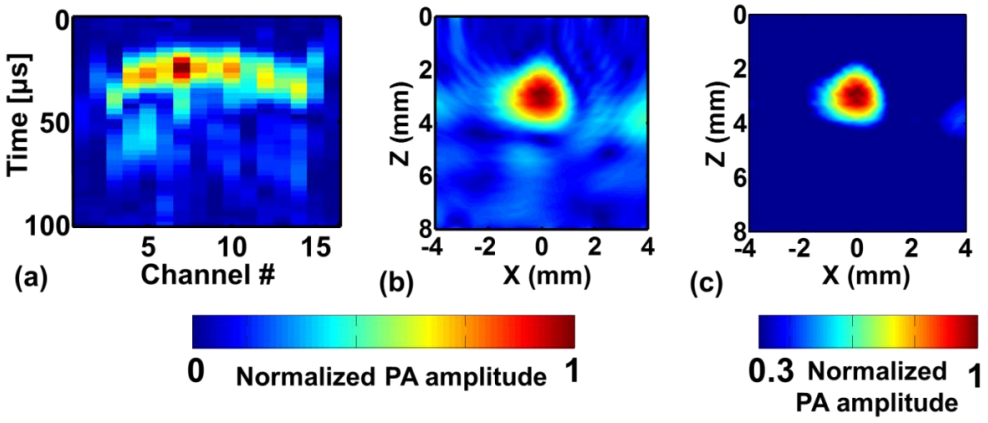

Figure 14 PA image reconstruction. (a) Rearranged Hilbert-transformed raw data acquired by 16 optical fibers; (b) Reconstructed PA imaged with compensation for the acoustic attenuation in each fiber; and (c) Thresholded (30%) PA image of (b) [83]. Reprinted with permission © 2014 by JBO.

3.5 Conclusion

In this work, we have successfully demonstrated a hand-held PAT probe using optical-fiber PADLs. To minimize their layout space, laser-micromachined spacer structures were used to wind the optical-fiber PADLs into spiral coils with suitable radii of curvature. Thus, all 16 optical-fiber PADLs fit into a compact probe structure suitable for handheld operation. By properly designing and constructing the micro spacer structures and carefully threading the optical fibers, we achieved robust and accurate placement of the optical-fiber PADLs with small acoustic distortion and inter-channel coupling. Using the hand-held PADL probe, 16 channels of PA signals can be unambiguously received with two single-element transducers and two DAQ channels, which corresponds to a channel reduction ratio of 8:1. The handheld PADL probe could be used to conduct real-time PAT without a complex ultrasound receiver system.

It should be noted that using optical fibers as the PADLs has some drawbacks. To achieve higher lateral imaging resolution, a larger number of PADLs are desired. However, as the number of PADLs increases, the optical fibers will become longer and the acoustic attenuation will be higher, which will also make the probe assembly process more complex and labor-intensive. A second issue is the uncontrolled ultrasound detection angle due to the small diameter of the optical fiber (e.g., 100~200 μm). To receive the PA signals within a well-controlled detection angle requires a larger size (e.g., ~mm) of the input terminal. In the future, new PADL materials, designs and construction methods will be investigated to address these issues and also to improve the PA imaging capability (e.g., a larger number of channels and higher channel reduction ration).

4. MICROMACHINED SILICON PADL FOR REAL-TIME PHOTOACOUSTIC TOMOGRAPHY*

4.1 Probe design and construction

4.1.1 Design

Due to the high acoustic velocity (~8430 m/s [91]) of silicon, an acoustic delay length ranging from a few to tens of centimeters is necessary to provide suitable acoustic time delays (1–10 μs) between two adjacent PADLs, so that the PA signals do not overlap with each other and therefore can be clearly distinguished when they reach the single-element transducer [93]. To achieve a compact structure, the PADLs were designed as tightly wound spiral coils.

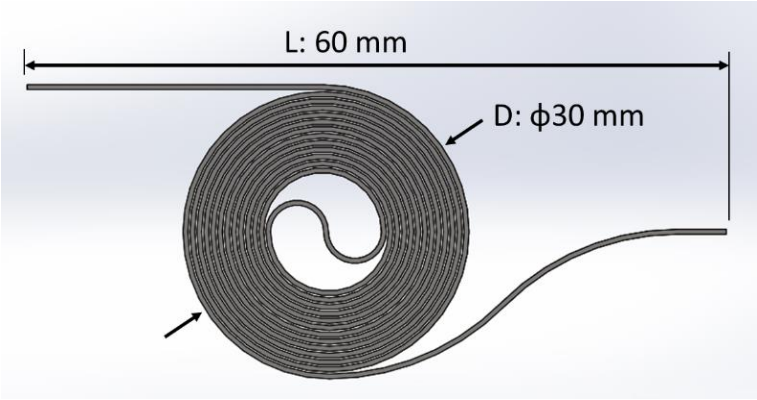

Figure 15 Schematic design of the longest (16th) silicon PADL [84]. Reprinted with permission © 2016 by JOPT.

* Part of this section is reprinted with a permission from "Micromachined silicon parallel acoustic delay lines as time-delayed ultrasound detector array for real-time photoacoustic tomography" Cho Y, Chang CC, Wang LV, Zou J. 18(2):024003 [84] © 2016 by JOPT and "A micromachined silicon parallel acoustic delay line (PADL) array for real-time photoacoustic tomography (PAT)" Cho Y, Chang CC, Wang LV, Zou J. [85] © 2015 by SPIE.

Figure 15 shows the schematic design of the longest (the 16th) PADL. The diameter of its circular portion is 30 mm, which is still compact even though its delay length reaches 90 cm. All 16 PADLs have the same span of 60 mm between their input and output terminals (L in Figure 15), which facilitates the assembly and ease of contact between the imaging target and the single-element transducer.

Table 3 Main design parameters of silicon PADLs [84]. Reprinted with permission © 2016 by JOPT.

Parameter	Value
number of channels	16
shortest delay	9.5 μs
longest delay	107 μs
incremental delay	6.5 μs
center frequency	2.25 MHz
cross section	500 μm × 250 μm
minimum radius of curvature	2 mm

Table 3 lists the main design parameters of the silicon PADL array. The shortest and longest acoustic time delays are 9.5 μs and 107 μs, respectively. The nominal incremental acoustic time delay between any two adjacent channels is 6.5 μs, which corresponds to a penetration depth of ~1 cm in soft tissue (assuming an acoustic velocity of ~1500 m/s). The cross-sectional area of the silicon PADLs is 500 μm × 250 μm, which

provides good mechanical stiffness (and therefore structural stability) and also good acoustic signal transmission for PA signals. For a rectangular acoustic delay line, its width or thickness (d) (whichever is smaller) should satisfy (df/V_0) << 1 to avoid signal distortion due to higher-order mode propagation and mode dispersion, where f is the frequency of the signal, and V_0 is the acoustic velocity of the delay-line material [90]. Assuming the silicon PADLs are interfaced with a single-element ultrasonic transducer with a center frequency of 2.25 MHz and a bandwidth of 100%, the maximum detection frequency will be 3.375 MHz. This value yields a df/V_0 ratio of 0.1 (<<1) to ensure single-mode transmission of the PA signals with minimal mode dispersion. Based on our previous simulation and experimental characterization results [93], the smallest radius of curvature in the center portion of the PADL structure was made larger than 2 mm to ensure high acoustic transmission efficiency by reducing mode conversion at curved sections of the acoustic delay lines.

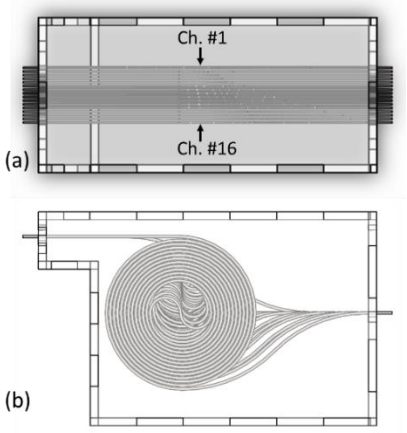

Figure 16 The assembly of 16-channel silicon PADL array. (a) Top view (b) side view [84]. Reprinted with permission © 2016 by JOPT.

Figure 16 shows a 3-D design of the assembled 16-channel silicon PADL array with one common input port and one common output port. During PA imaging, the input port is in contact with the imaging target, and all 16 channels detect the incoming PA signals simultaneously. The output port is interfaced with a single-element transducer to receive the transmitted PA signals.

4.1.2 Fabrication and assembly

The silicon PADLs were fabricated on 4-inch [45]-oriented single crystal silicon wafers with a thickness of 250 μm (University Wafers, Boston, MA, USA) by using a microfabrication process developed previously [93]. First, a 300 nm-thick aluminum layer was deposited on the silicon wafers by electron-beam evaporation. Second, the deposited aluminum layer was patterned by photolithography and wet etching, forming a mask for silicon etching. Third, the silicon PADL structures were directly formed on the silicon wafers by removing unwanted regions with deep reactive ion etching (DRIE). In the last step, the etched PADL structures were separated from each other for final assembly.

To precisely position the silicon PADLs in the array at the input and output ports, two identical spacer structures were laser cut from a 0.4 mm thick clear acrylic sheet using the laser engraving and marking machine (PLS6.75, Universal Laser Systems, Scottsdale, AZ, USA) (Figure 17). Each spacer structure consists of 16 shallow trenches (300 μm × 500 μm) to support the silicon PADLs and 15 interspaced deep trenches (200 μm × 1000 μm) to reduce acoustic crosstalk between adjacent supports. Both the shallow and deep trenches were formed by using a dicing saw. To protect the entire silicon PADL array, an

acrylic housing was also fabricated (see Figure 16). Its top panel, bottom panel, and two side walls were laser cut from a 1.5 mm thick acrylic sheet.

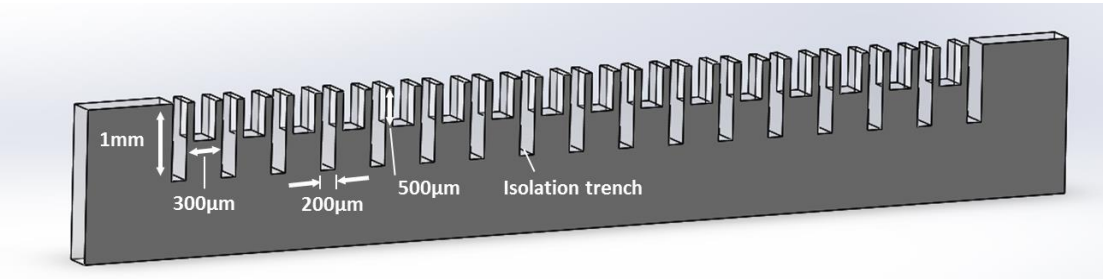

Figure 17 Design for spacers of the input and output port [84]. Reprinted with permission © 2016 by JOPT.

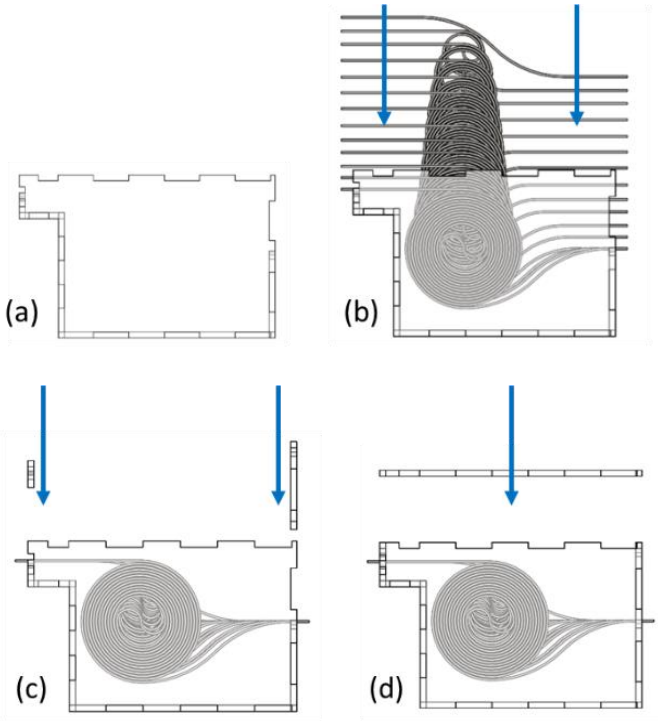

Figure 18 Assembly process of the PADL array. (a) Assembling two sidewalls, bottom, front, back, and spacers. (b) Arranging and placing 16 PADLs. (c) Fastening PADLs (d) Affixing top panel [84]. Reprinted with permission © 2016 by JOPT.

The assembly process of the silicon PADL array is illustrated in Figure 18. First, the bottom panel, side panels, and the two spacers were bonded together with acrylic cement, then the 16 silicon PADLs were placed in the spacer grooves. The PADLs were fastened with two small parts for mechanical stability. In the last step, the top panel was cemented in place to form a sealed housing. The input and output ends were polished to ensure uniform contact with both the imaging target and the ultrasonic transducer. Figure 19 shows the fully assembled 16-channel silicon PADL array.

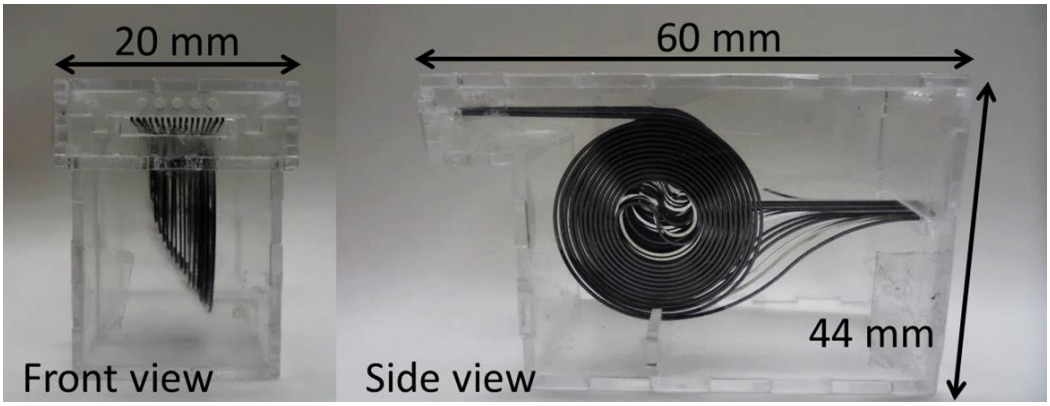

Figure 19 Fully assembled 16-channel silicon PADL array [85]. Reprinted with permission © 2016 by JOPT.

4.1.3 The acoustic acceptance angle of silicon PADLs

For PA imaging, the acceptance angle of the detector is an important factor to determine the spatial resolution. Based on the principle of reciprocity, the detection pattern of a detector is the same as its radiation pattern. The silicon PADLs can be treated as a

linear array with a small element separation (*b*) (Figure 20a). The directivity factor of its far-field radiation pattern in the lateral direction can be estimated by

$$D(\theta) = \frac{\sin((\pi d / \lambda)\sin\theta)}{(\pi d / \lambda)\sin\theta} \qquad \text{(Equation 3)}$$

where *d* is the total width of the linear array in the lateral direction, λ is the ultrasound wavelength, and θ is the angle relative to the normal direction of the linear array [96]. Figure 20b shows the calculated directivity factor of the 16-channel silicon PADLs (with a total width *d* of 9 mm) in water at the frequency of 2.25 MHz. The radiation power quickly drops to less than –20dB when θ reaches 4°, which indicates a small acceptance angle in the lateral direction.

Since all the PADLs have the same detection pattern in the elevational direction, the acceptance angle in the elevational direction the silicon PADLs can be determined with a single delay line from Equation 3 (Figure 21a), where *d* represents the width (500 μm) of the single delay line. Figure 21b shows the calculated directivity factor of a single delay line in water at the frequency of 2.25 MHz. The radiation power only drops to -6 dB when θ reaches 55.7°, which indicates a large acceptance angle. This is mainly due to the relatively small element size compared with the ultrasound wavelength in water at 2.25 MHz. To better understand and visualize the radiation pattern, a numerical simulation was conducted to estimate the ultrasound propagation and radiation from single delay line by using Wave 2500® (CyberLogic, Inc., New York, NY, USA).

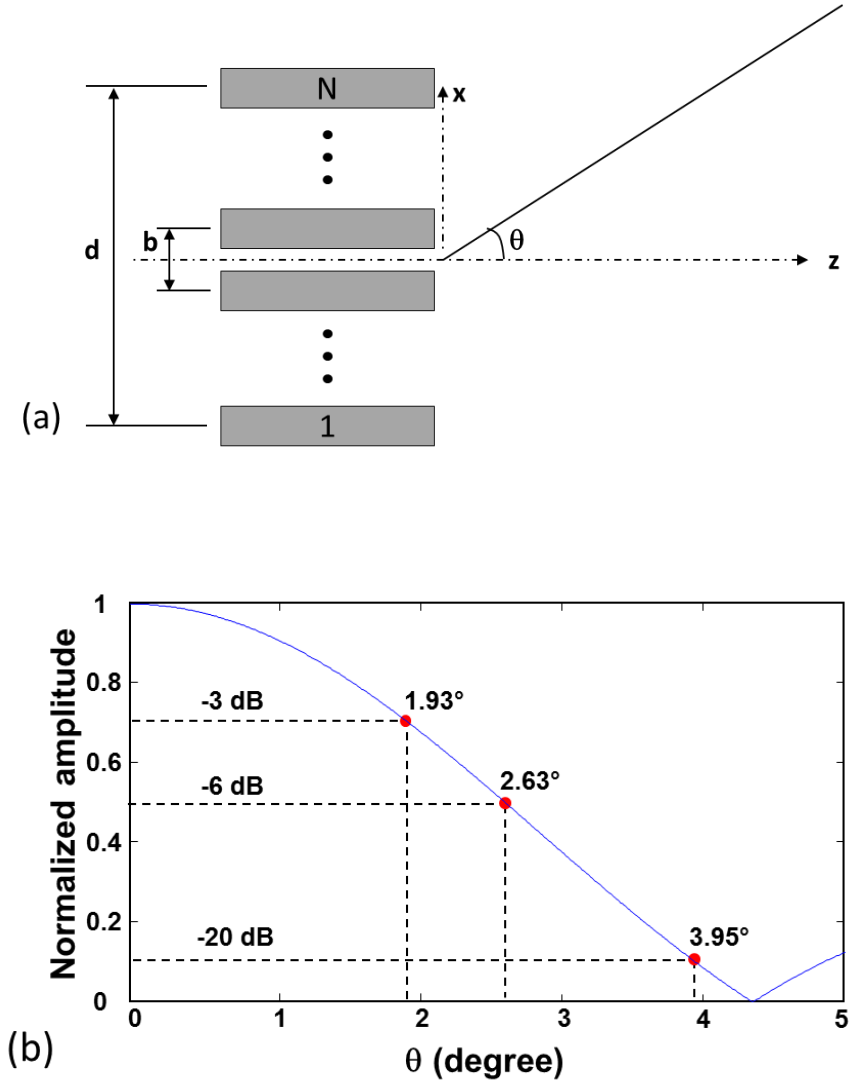

Figure 20 Directivity factor of a linear array. (a) A linear array of PADLs (b) the directivity factor in the lateral direction calculated from Equation 3 [84]. Reprinted with permission © 2016 by JOPT.

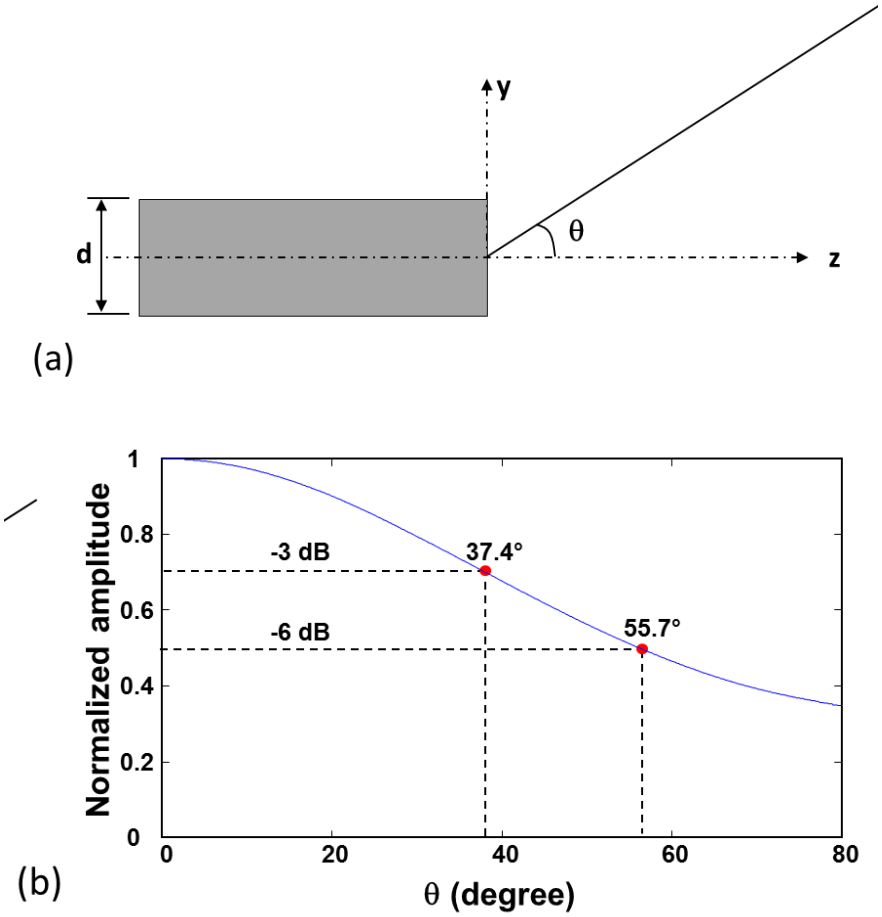

Figure 21 Directivity factor of a single delay line. (a) A single PADL (b) the directivity factor in the elevation direction calculated from Equation 3 [84]. Reprinted with permission © 2016 by JOPT.

Thirty-one virtual ultrasound receivers were used to measure the radiation power at different angles ranging from 0 to 90° (Figure 22a). The directivity factor of single silicon PADL was determined based on the measured radiation power (Figure 22b), which matches well with that calculated from Equation 3 (Figure 21b).

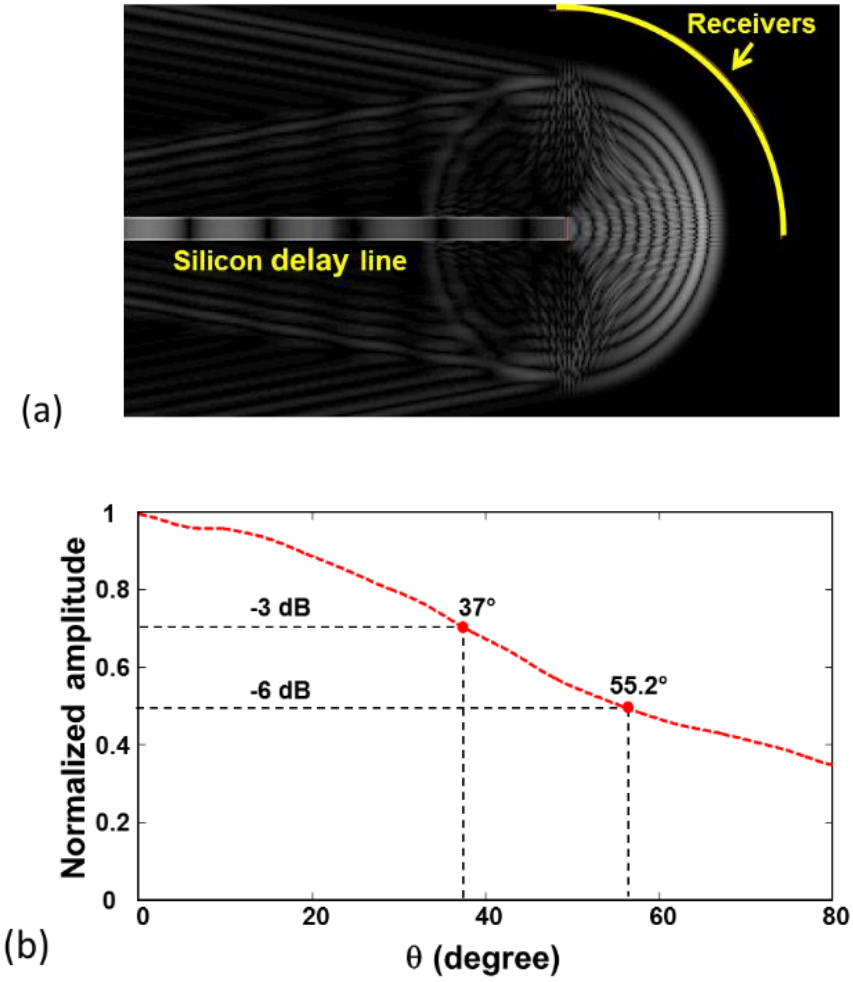

Figure 22 Simulation results of a single delay line. (a) The simulated radiation pattern of single silicon delay line in Wave 2000® (b) the directivity factor estimated from the simulation data [84]. Reprinted with permission © 2016 by JOPT.

4.2 Ultrasonic characterization and PA imaging

4.2.1 Ultrasonic testing setup

A two-port ultrasound testing setup was built to characterize the acoustic transmission properties of the assembled silicon PADL array (Figure 23). Two 2.25 MHz transducers (V104, Olympus NDT, Waltham, MA, USA) were used to transmit and

receive the ultrasound signals. The input and output ports of the silicon PADL array were placed in contact with the transmitting and receiving transducers, respectively. Mineral oil was applied to both ends of the silicon PADLs and the surfaces of the transmitting & receiving transducers to enhance the coupling efficiency and minimize unwanted reverberation. The pulser/receiver (5072PR, Olympus NDT, Waltham, MA, USA) was set to transmission mode and sent a driving voltage pulse to the transmitting transducer, which both generated ultrasound signals and also amplified signals detected by the receiving transducer. The ultrasound signals from the transmitting transducer traveled from the input port to the output port through the 16-channel silicon PADLs with distinctly different amounts of time delay. To improve the SNR (signal-to-noise ratio), all 16 channels of ultrasound signals were averaged 16 times and recorded on a digital oscilloscope (TDS2014B, Tektronix Inc., Beaverton, OR, USA).

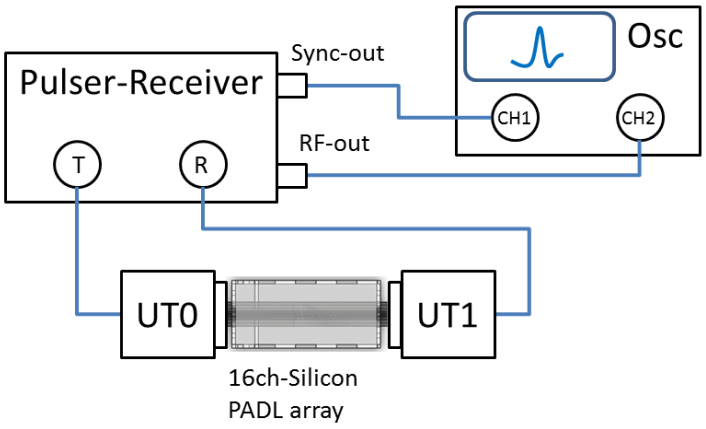

Figure 23 A two-port ultrasound testing setup with the 16-channel silicon PADL array. Osc: Oscilloscope. UT0, UT1: Ultrasonic transducers 0 and 1 [84]. Reprinted with permission © 2016 by JOPT.

4.2.2 PA imaging setup

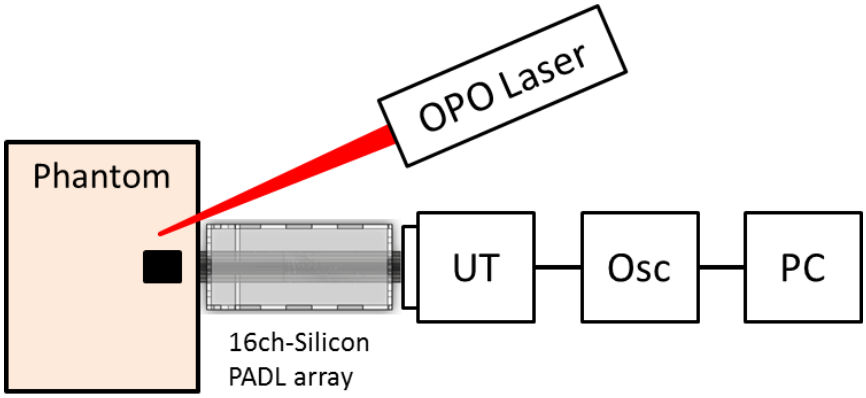

Figure 24 PA imaging setup with the 16-channel silicon PADL array [84]. Reprinted with permission © 2016 by JOPT.

Figure 24 shows the experimental setup of the PA imaging experiment. A frequency-doubled Q-switched 532-nm Nd:YAG laser (LT-P100, Mychway Technology Co., Limited, Shenzhen, Guangdong, China) was the light source. The laser pulse duration was 8 ns and the pulse repetition rate was 5 Hz. The imaging target was a piece of silicon (1 mm × 0.25 mm × 1 mm) embedded in an optical tissue phantom (100 mm × 100 mm × 50 mm). The phantom was composed of 2% agar gelatin by weight, and the target was located 2.5 mm below the phantom surface. The PA signals generated from the imaging target propagated along the silicon PADL array and were received by a single-element 2.25 MHz ultrasonic transducer (V106, Olympus NDT, Waltham, MA, USA), then amplified by a pulser/receiver (5072PR, Olympus NDT, Waltham, MA, USA). The

amplified PA signals were averaged five times and then recorded on a digital oscilloscope (TDS2014B, Tektronix Inc., Beaverton, OR, USA) at a sampling rate of 5 MHz.

4.2.3 PA data acquisition and image reconstruction

The PA signals were averaged five times to generate one PA image; thus the imaging speed was 1 Hz. The end of each PADL on the sample surface was considered as a single element in an ultrasound array. Each sequentially detected PA signal was reshaped into 16 separate PA signals, based on the predefined time positions measured by the ultrasound transmission experiment. To reconstruct PA images, a commonly used delay-and-sum beamforming method was applied [35]. The PA images were reconstructed by summing the data from all 16 channels after compensating for the time delays in each silicon PADL, based on its length and matching phase. In a two-dimensional beam field along the x and z directions, the time delay τ_n for the n^{th} PADL located on (x_n, z_n) can be calculated as follows:

$$\tau_n = \frac{\sqrt{(x - x_n)^2 + (\mathrm{z} - \mathrm{z}_n)^2} - R}{c} \qquad \text{(Equation 4)}$$

where R is the distance from the focal point to the center of the delay line, and c is the speed of sound in soft tissue, 1540 m/s. Envelope detection was applied by using Hilbert transformation along the axial direction (the *z*-direction), followed by taking the absolute value.

4.3 Results and discussion

4.3.1 Ultrasonic transmission through the silicon PADL array

Figure 25a shows the 16 channels of time-delayed ultrasound signals received by the single-element ultrasonic transducer. The acoustic delay in each ultrasound signal was determined by measuring the time interval between its peak intensity and that of the trigger signal (Figures 25b and 25c). The average incremental acoustic delay between two adjacent channels was ~7 μs, slightly longer than designed value of 6.5 μs. This difference is due to the fact that when they travel in the curved portion of the silicon PADLs, the ultrasound signals encounter multiple reflections on the sidewalls. As a result, their velocity is different from that in a straight line and their actual travel distance is longer than the length of the silicon delay lines. The acoustic attenuation was determined based on the change in the amplitude of the ultrasound signals as they propagated through different distances. Theoretically, acoustic attenuation varies linearly with the length of the silicon PADLs, but the amplitudes of the received ultrasound signals showed otherwise. One possible reason could be non-uniform contact between the silicon PADLs and the two ultrasound transducers. Here, the average acoustic attenuation of the silicon PADLs was calculated by measuring the signal amplitude difference between the shortest (1st) and the longest (16th) PADL. It was 0.058 dB/cm @ 2.25 MHz, which is higher than that in a straight silicon delay line (0.015 dB/cm @ 2.25 MHz) [93]. As observed in our previous experiments [93], when ultrasound signals travel along a curved delay line, they encounter more reflections and potential mode conversions on the sidewall of the delay line, which

contribute to higher acoustic attenuation. However, it should be mentioned that the attenuation of 0.058dB/cm is still very low, and can be neglected.

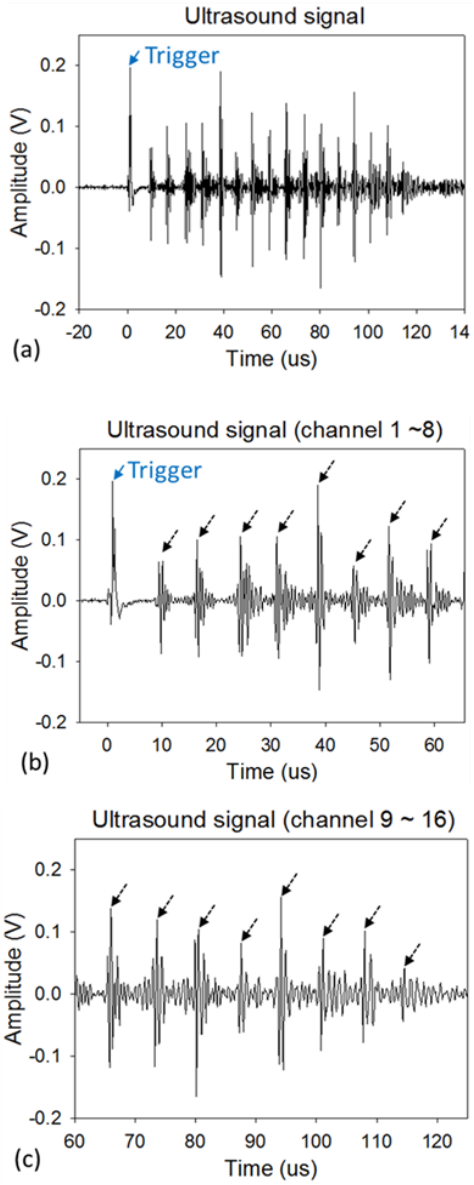

Figure 25 2.25 MHz ultrasound signals propagating through the 16 silicon PADLs. (a) A trigger and 16 signals. (b) Zoomed-in view of a trigger and the eight signals from channels 1 to 8. (c) Zoomed-in view of the eight signals from channel 9 to 16 [84] . Reprinted with permission © 2016 by JOPT.

4.3.2 PAT imaging

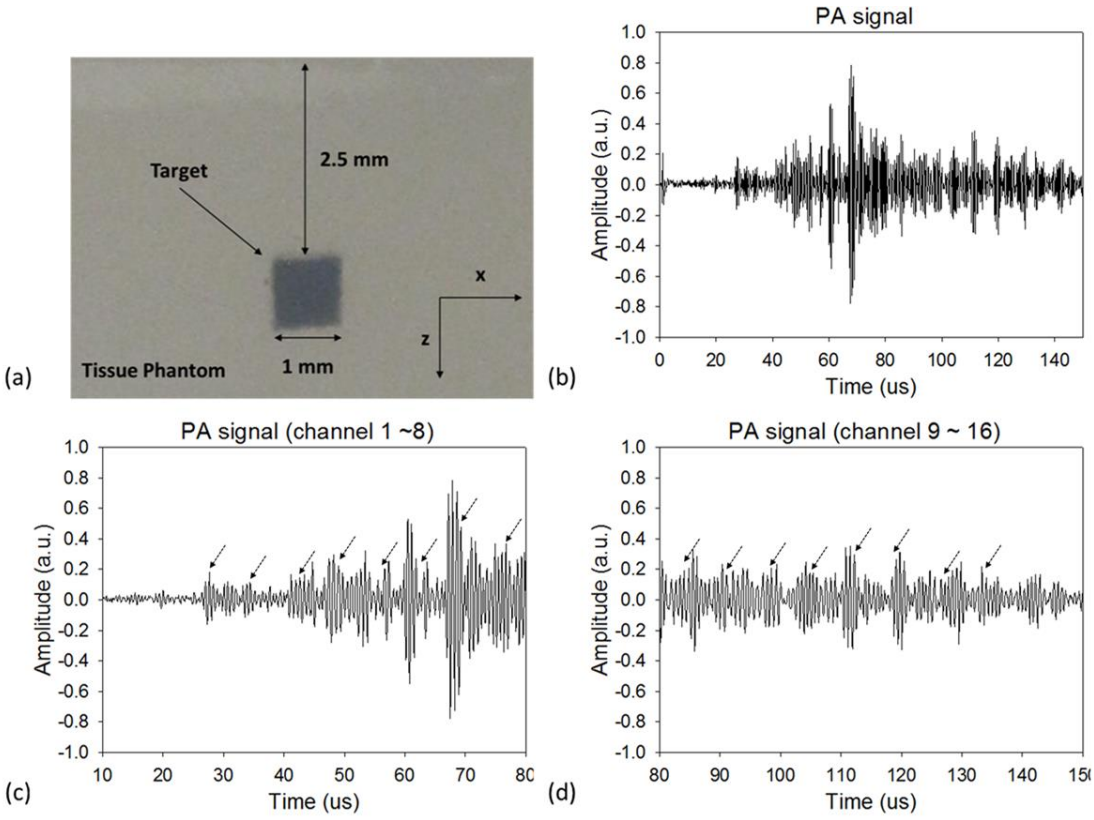

Figure 26 PA imaging phantom and raw PA signals received by an ultrasonic transducer. (a) Photography of an optically absorbing target embedded in an optically scattering medium. (b) PA signals received by the ultrasonic transducer through the 16 silicon PADLs. (c) Zoomed-in view of the eight signals from channel 1 to 8. (d) Zoomed-in view of the eight signals from channel 9 to 16 [85]. Reprinted with permission © 2015 by SPIE.

Figure 26a shows the tissue phantom with a piece of silicon target located 2.5 mm below the phantom surface. Figures 26b, 26c, and 26d show the 16 PA signals from the silicon PADL array acquired by the single-element ultrasound transducer and the DAQ channel after five times averaging. Each PA signal was identified based on the time delay

(7 μs) previously determined in ultrasound transmission testing. Figure 27 shows the reconstructed PA image in Matlab®. The envelope of the PA signals was detected by using Hilbert transformation, and the PA image was reconstructed using the synthetic aperture focusing technique (SAFT) [97] to improve spatial resolution. As shown in Figure 27a, in the reconstructed PA image, both the location and the size of the imaging target match the actual values. The image contrast, defined as $(PA_{target} - PA_{background})/ PA_{background}$, is calculated to be ~1.9. The spatial resolution, defined as the one-way distance between 10% and 90% of the maximum, divided by the minimum, is ~2.1 mm. Figure 27b shows the enhanced PA image after applying a signal threshold of 30%.

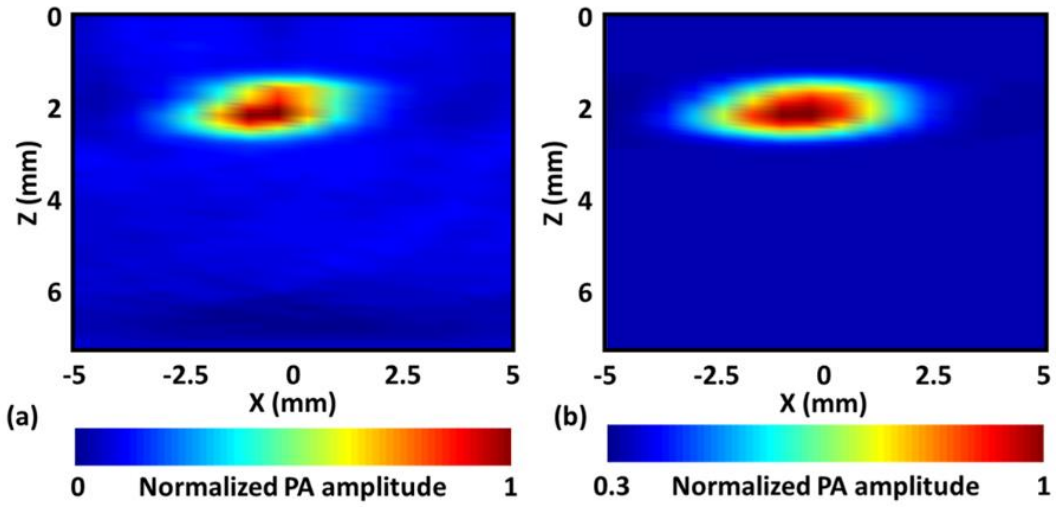

Figure 27 Reconstructed PA images. (a) Reconstructed PA image of the imaging target. (b) Thresholded (30%) PA image of (a) [85]. Reprinted with permission © 2015 by SPIE.

4.4 Conclusion

In this work, we have successfully demonstrated a micromachined silicon PADL array for real-time PAT. The array capitalizes upon the extremely low acoustic loss of single-crystalline silicon and the high precision of the micromachining process. Using the silicon PADL array, a transducer/channel reduction ratio of 16:1 was achieved, which is twice what was obtained previously with optical-fiber PADLs. In the future, larger silicon PADL arrays will be investigated to provide even higher transducer/channel reduction ratios to fulfill the potential of the time-delayed ultrasound reception approach. In addition, new solutions will be developed to improve the sensitivity, the acoustic acceptance angle in the elevation direction, and impedance matching at the input terminals to obtain better PA signal detection.

5. MICROMACHINED SILICON ACOUSTIC DELAY LINE WITH 3D-PRINTED MICRO LINKERS AND TAPERED INPUT FOR IMPROVED STRUCTURAL STABILITY AND ACOUSTIC DIRECTIVITY*

5.1 Design of a silicon acoustic delay line and 3D-printed micro linker

5.1.1 Improving structural stability

As shown in Figure 15, the micromachined silicon acoustic delay lines were designed into closely-wound coils to provide a compact structure. To illustrate the structural instability issue, finite-element simulations were conducted with Solidworks® (Dassault systems Americas Corp., Waltham, MA, USA) to study the mechanical deformation of a representative silicon acoustic delay line structure under its own weight. The acoustic delay line has a total delay length of 1570 mm and a total delay time of ~186 μs (based on an acoustic velocity of ~8454 m/sec determined in our previous work [93]), respectively. For comparison, the longest delay line in the array shown in Figure 15 only has a delay length of 904 mm and a delay time of ~107 μs, respectively. The mechanical properties and geometric parameters used in the simulation are listed in Table 4. As shown in Figure 28a, when being supported at its two ends, the delay line structure collapses even under its own weight. The excessive amount of deformation occurring at the bottom portion creates direct contacts between adjacent turns, which would cause significant acoustic crosstalk and signal distortion. The mechanical deformation of the same acoustic

* Part of this section is reprinted with a permission from "Micromachined silicon acoustic delay line with 3D-printed micro linkers and tapered input for improved structural stability and acoustic directivity" Cho Y, Kumar A, Xu S, Zou J. 26(10):105003 [86] © 2016 by JMM.

delay line structure was simulated again after adding four linker structures to restrain the vertical and lateral movement of the adjacent turns. As shown in Figure 28b, the mechanical stiffness and the structural stability of the acoustic delay line structure can be significantly improved with the application of the four linker structures.

Table 4 Mechanical properties and geometric parameters of the simulated silicon acoustic delay line [86]. Reprinted with permission © 2016 by JMM.

Mechanical Properties and Parameters	Value
Elastic modulus	112.4 GPa
Poisson's ratio	0.28
Shear modulus	49 GPa
Mass density	2330 kg/m^3
Delay line cross section	500 μm x 280 μm
Delay line length	1570 mm
Delay time	186 μs
Gap between adjacent turns	500 μm
Overall length	49.5 mm
Overall width	40.5 mm

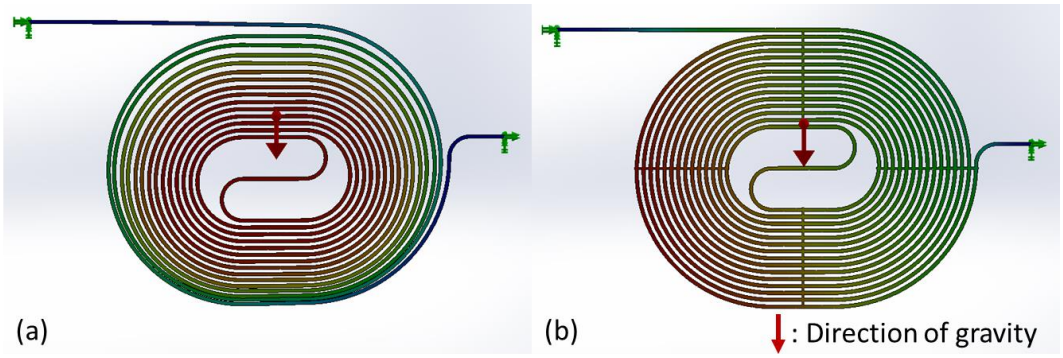

Figure 28 Simulated structural deformation of a silicon acoustic delay line under its own weight (a) without linker structure and (b) with four linker structures [86]. Reprinted with permission © 2016 by JMM.

To apply the linker structures onto the silicon delay line, the most straightforward way is to modify the mask layout design for patterning the delay line structure, such that both the linkers and delay lines are formed together in one step. However, because both the linker and delay line structures are made of the same (silicon) material, significant acoustic coupling between two adjacent turns of the delay line structure could occur. Therefore, it would be best if the linker structures are made of other materials with significantly different acoustic properties, such as polymers. To evaluate the acoustic coupling caused by the linker structures, numerical simulation was conducted using a commercial ultrasound simulation software Wave2000® (CyberLogic, Inc., New York, NY, USA) on a group of four straight parallel silicon delay lines with different types of linker structures. The software uses a time domain finite difference method to solve the 2D acoustic wave propagation in the media [98]. One acoustic source was applied to the left end of the first silicon delay line and four receivers were placed on the right ends of the four delay lines. The acoustic source applied to the silicon delay line was a single sine

Gaussian pulse with an amplitude of 0.5 V, a duration of 6 μs, and a frequency of 2.25 MHz. The acoustic properties of materials used in this simulation are summarized in Table 5. We chose a polyester casting resin from the material library in Wave2000® as a polymer material for simulation. Figures 29a and 29b show the simulated wave propagation in the four delay lines with silicon linkers and the ultrasound signals detected by the receivers, respectively. It is clearly shown that due to high acoustic coupling through silicon linker structures, the signal crosstalk was detected by the receiver 2, 3, and 4, and a weaker transmission signal was received at the receiver 1. Based on the simulation data, the crosstalk through the silicon linker structures was calculated to -13 dB. Figures 30a and 30b show the simulated wave propagation in the four delay lines with polymer linker structures and the ultrasound signals detected by the receivers, respectively. From the simulation data, the crosstalk through the polymer linkers was calculated to -55 dB. For comparison, the acoustic crosstalk between two adjacent elements in a conventional piezoelectric transducer array is around -35 dB [99]. Therefore, the polymer linkers can provide good acoustic isolation for the silicon delay lines.

Table 5 Acoustic properties used in Wave2000 simulation [86]. Reprinted with permission © 2016 by JMM.

Acoustic Properties	Silicon	Air at 20°C	Polymer
Density (kg/m^3)	2330	1.24	1070
Speed of sound (m/s)	8430	344	2289
Acoustic impedance (MRayl)	19.7	0.000426	2.45

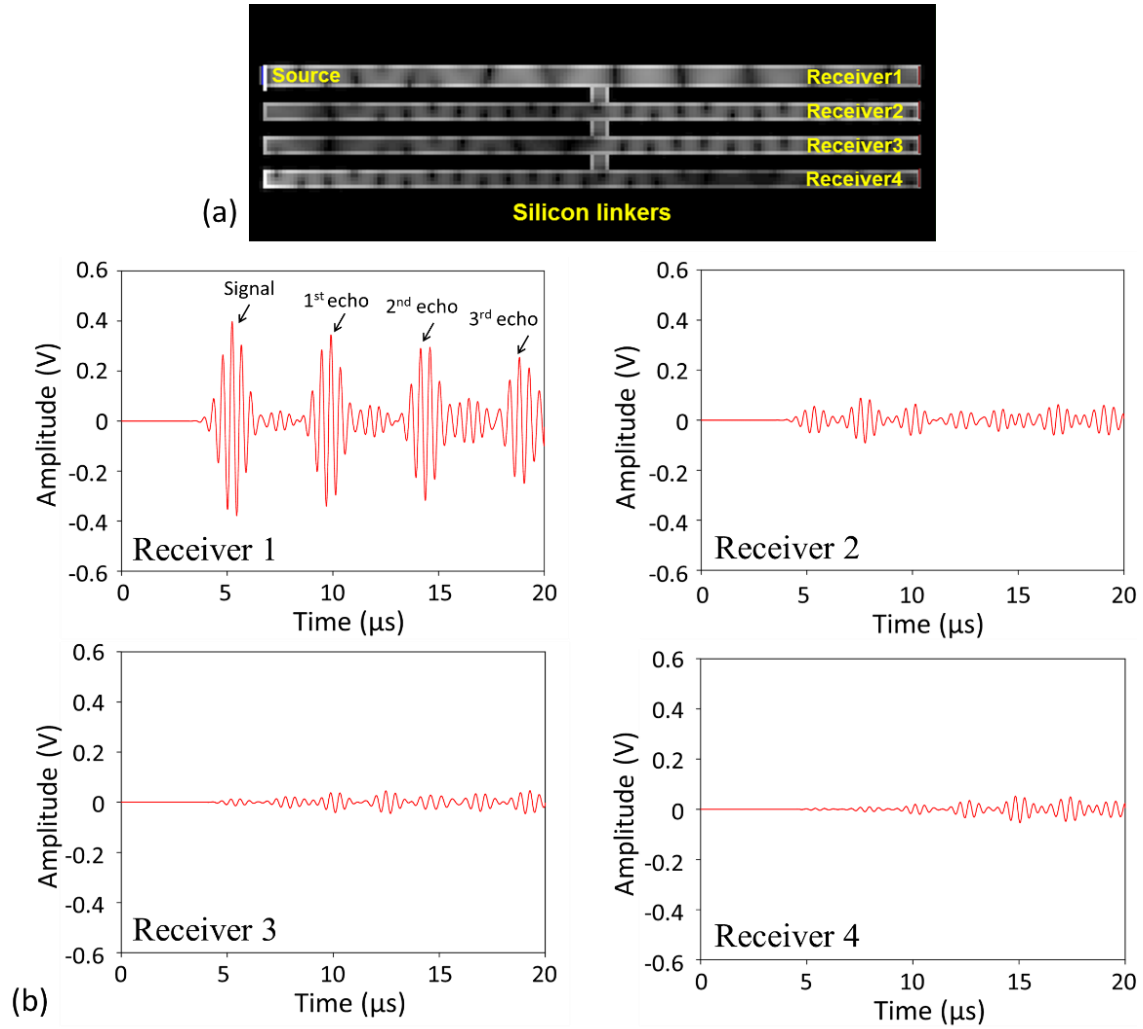

Figure 29 Wave2000® simulation of acoustic signal transmission through four straight silicon delay lines with silicon linker structures (a) acoustic wave propagation in delay lines, and (b) acoustic signal received by Receivers 1 – 4 [86]. Reprinted with permission © 2016 by JMM.

To verify the simulation results, dummy linker structures made of cement adhesive was tested. The cement adhesive (3515C, Testors, Vermon Hills, IL, USA), which is for cementing clear polystyrene, was directly pasted into the gap between two

diced silicon wires (as straight acoustic delay lines) through a micro-stencil made by laser cutting. Ultrasound testing was then conducted to characterize the acoustic transmission

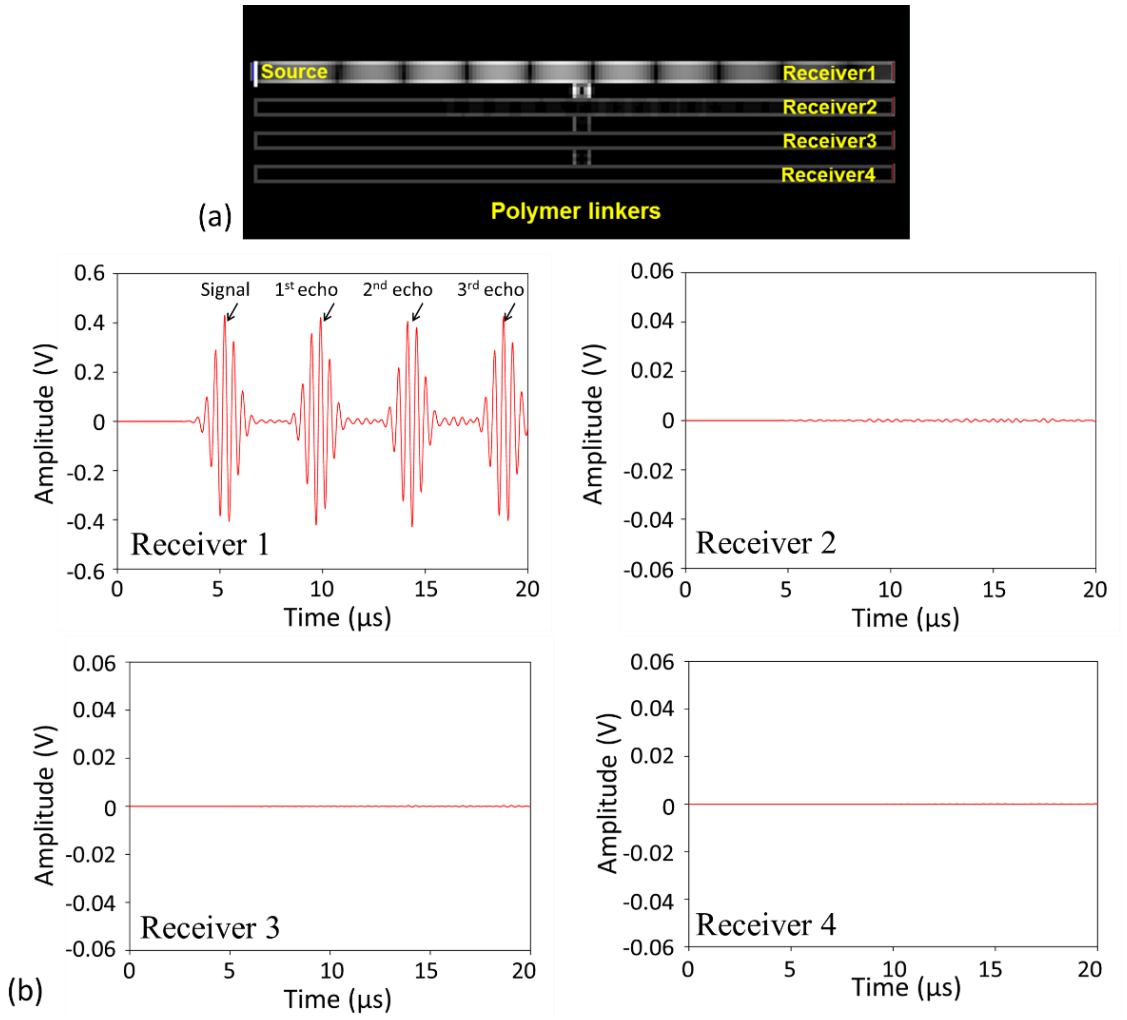

Figure 30 Wave2000® simulation of acoustic signal transmission through four straight silicon delay lines with polymer linker structures (a) acoustic wave propagation in delay lines, and (b) acoustic signal received by Receivers 1 – 4 [86]. Reprinted with permission © 2016 by JMM.

through the silicon delay line and the acoustic crosstalk through the solidified linker structures after the adhesive dried. The testing results show that although the acoustic

coupling through the linker structure is negligible, direct pasting adhesive onto the silicon delay line can cause significant attenuation in the acoustic transmission. To overcome this issue, the polymer linker structures were designed into individual locking hooks with open space inside and isolation trenches between (Figure 31). The space between locking hooks is made slightly larger than the dimension of the delay line structure to minimize direct contact points to reduce the unwanted attenuation. The isolation trenches are used to minimize signal crosstalk by providing enough space between each turn of silicon delay line. Once assembled onto the delay lines, the polymer linker structures can be held in place by the locking hooks without falling off.

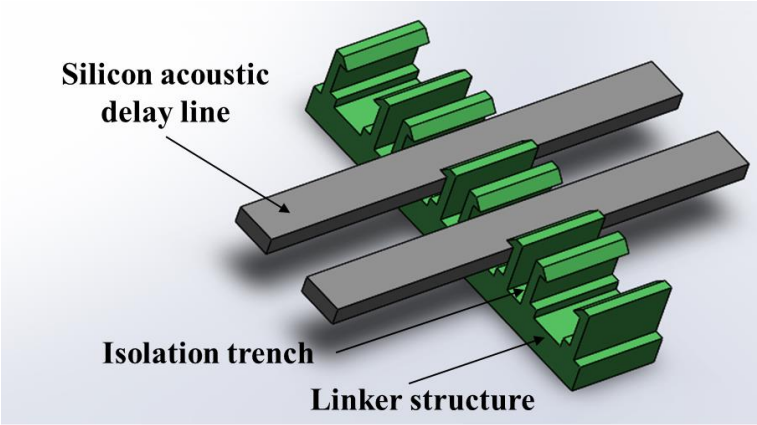

Figure 31 Design of the polymer micro linker structure [86]. Reprinted with permission © 2016 by JMM.

5.1.2 Improving acoustic acceptance angle

For PA imaging, the acoustic acceptance angle is an important factor to determine the spatial resolution. The acoustic acceptance angle can be evaluated with the directivity

factor. Silicon delay line array can be considered as a linear ultrasound array with a small element separation (*b*) (Figure 32). The directivity factor of its far-field radiation pattern in the lateral direction can be determined by

$$D(\theta) = \frac{\sin((\pi d / \lambda)\sin\theta)}{(\pi d / \lambda)\sin\theta} \qquad \text{(Equation 5)}$$

where d is the total width of the linear array in the lateral direction, λ is the ultrasound wavelength, and θ is the angle of radiation relative to the normal direction of the linear array [96]. Based on the principle of reciprocity, the detection pattern of a detector is the same as its radiation pattern [100]. Therefore, θ also refers to the angle of detection. The directivity factor indicates the relative ultrasound signal strength that can be either transmitted or received at a certain radiation or detection angle. The acceptance angle (θ) can be defined as the detection angle where the value of the directivity factor is reduced by -3 dB from its peak which occurs along the normal direction.

Figure 33 shows the -3dB acceptance angle for different d/λ ratios calculated from Equation 3. The acceptance angle decreases with a higher d/λ ratio, indicating better directivity. Because the total width (d) of the delay line array is usually much larger than the acoustic wavelength (λ), this leads to good directivity (i.e., small acceptance angle) along the lateral direction of the delay line array. However, in the elevational direction, the detection directivity and acceptance angle (ϕ) is determined by the width of one single delay line (h). To suppress high-order mode transmission and mode dispersion, the width

of the delay line needs to be kept as small as possible (e.g., $<<\lambda$), which inevitably leads to large acceptance angle and poor detection directivity. The acceptance angle of an acoustic detector can be changed by using acoustic lenses [101, 102]. However, for a small surface detector such as the silicon delay line, it is rather difficult to attach an acoustic lens onto its end. In addition, the acoustic lens could create abbreviation and additional impedance mismatch. Therefore, the input terminal of the delay line adopts a tapered design, in which the delay line starts with a larger width and gradually narrows down to its normal width. Different shapes and dimensions can be easily obtained just by changing the mask layout. Since Equation 3 does not apply to a tapered structure, numerical simulations were conducted in Wave2000® to estimate the elevational acceptance angle of the delay lines.

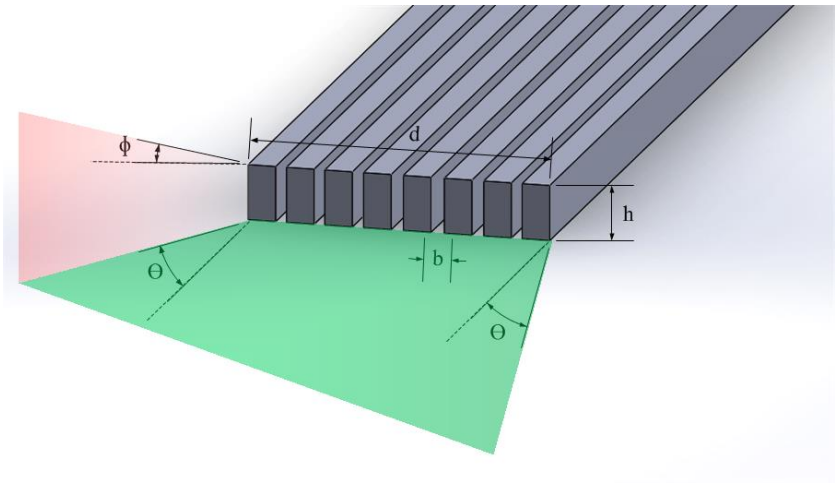

Figure 32 Radiation pattern of a linear array depending on geometry [86]. Reprinted with permission © 2016 by JMM.

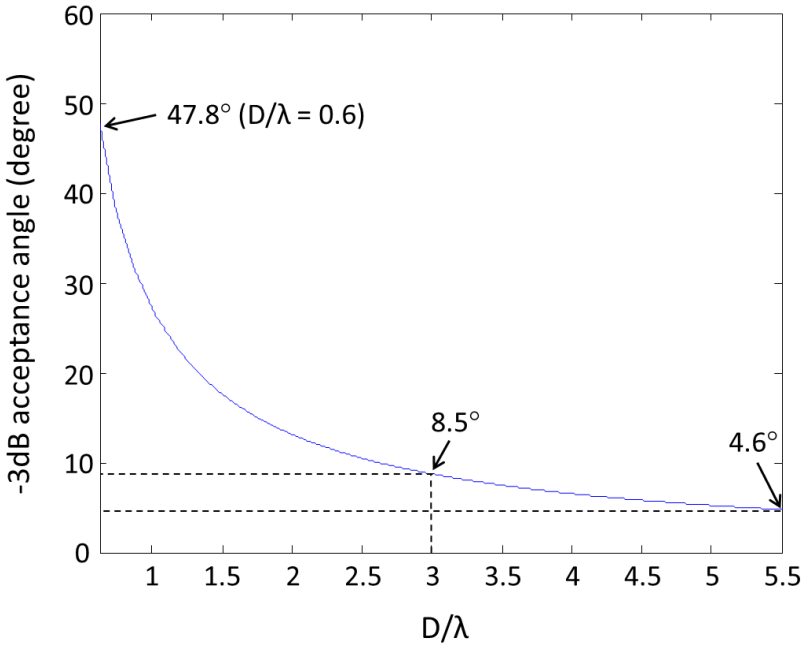

Figure 33 Acoustic acceptance angle changes for different d/λ [86]. Reprinted with permission © 2016 by JMM.

Table 6 Parameters used for radiation pattern simulation in Wave2000 simulation [86]. Reprinted with permission © 2016 by JMM.

Parameters	Value
Delay line length	20 mm
Width of the input terminal	0.5 mm, 1.5 mm, 3 mm
Number of ultrasound receiver	30

Figure 34 shows the simulated radiation patterns and directivity factors of the delay lines with different designs. When the width of the input terminal is increased from 0.5 mm to 3 mm, the -3 dB acoustic acceptance angle can be reduced from 37° to 13.3°. Parameters used for the simulation are listed in Table 6.

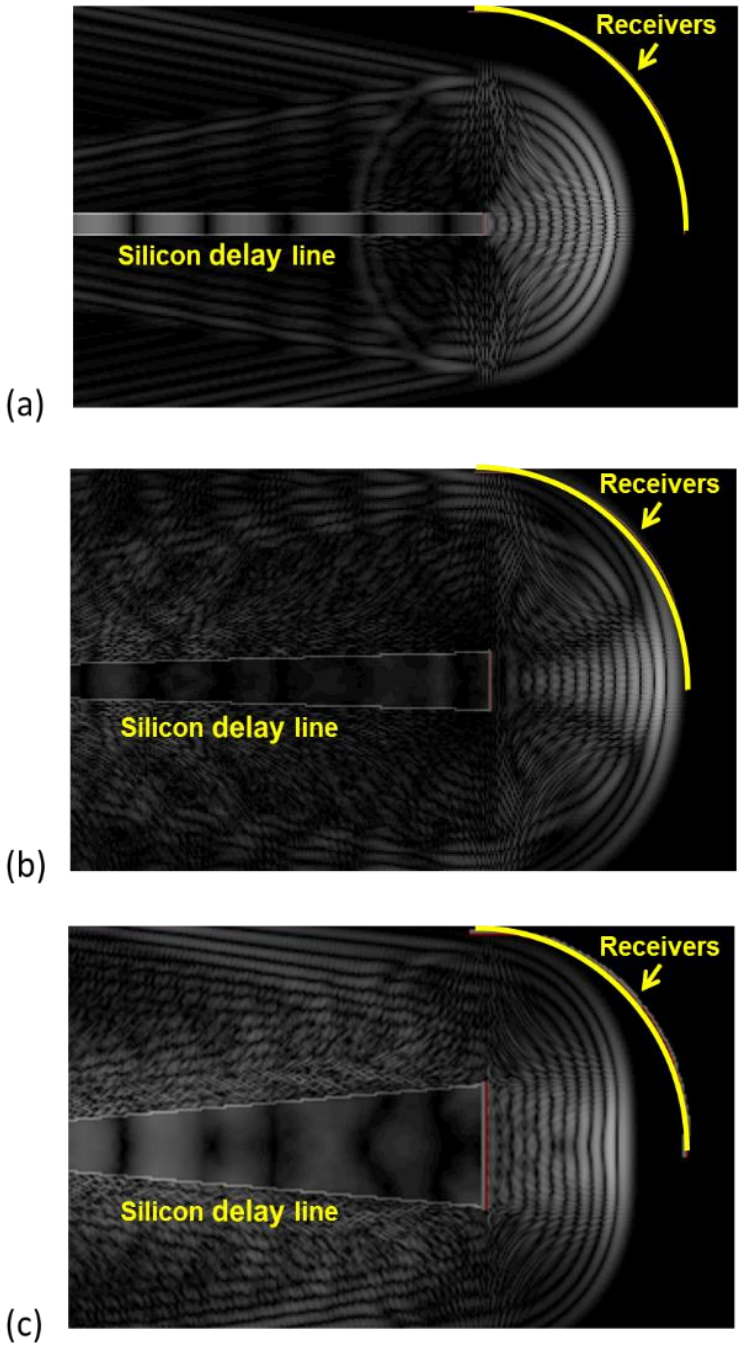

Figure 34 Simulation results of delay lines with different shapes. (a) The simulated radiation pattern of single silicon delay line (a width of 0.5 mm) in Wave 2500® [11] (b) a width of 1.5 mm, (c) a width of 3 mm; (d) the directivity factor estimated from the simulation data from (a), (e) from (b), and (f) from (c) [86]. Reprinted with permission © 2016 by JMM.

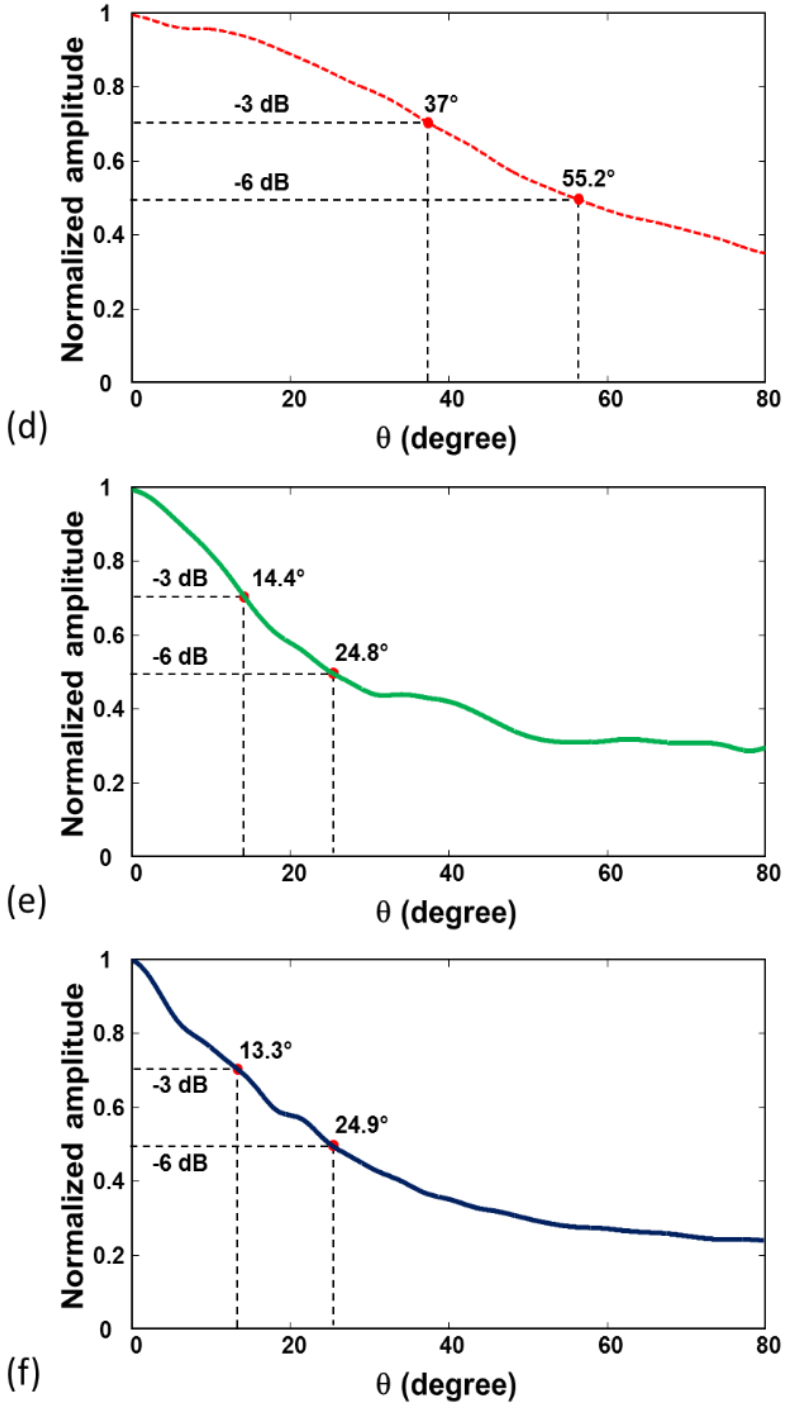

Figure 34 Continued.

5.2 Fabrication

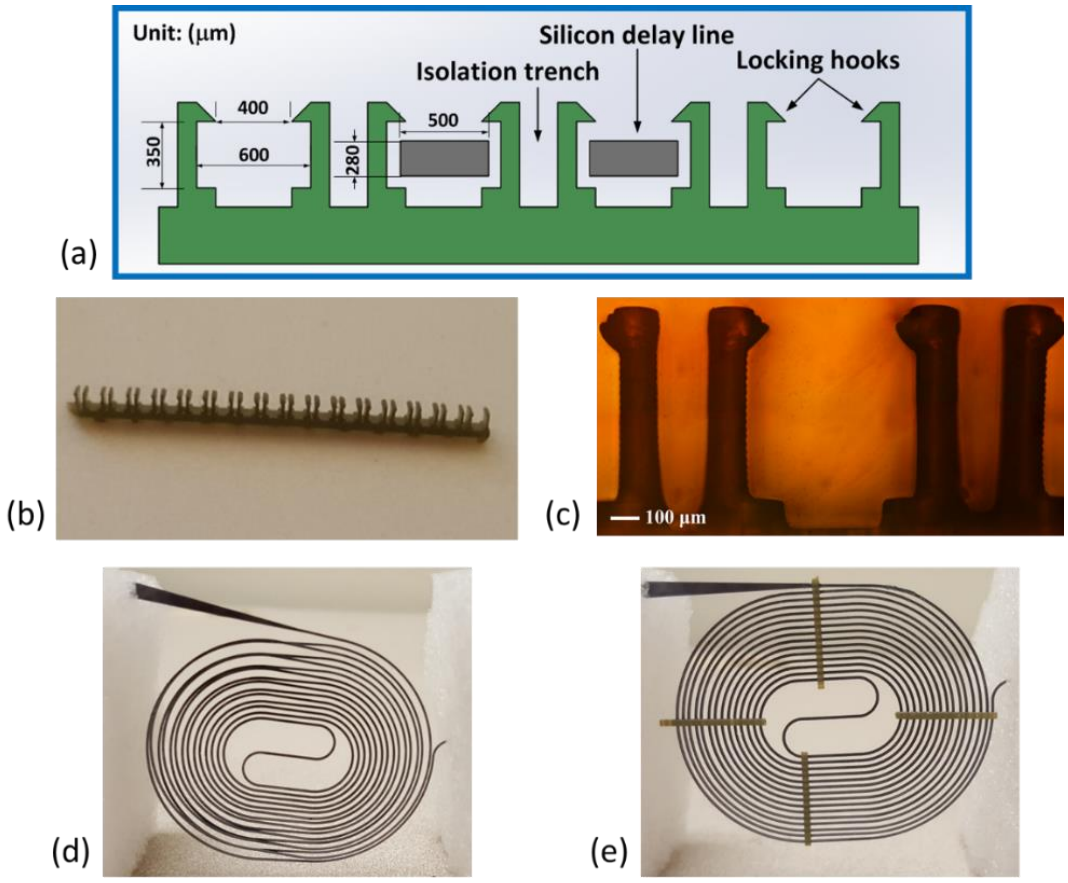

Figure 35 3D printed micro linker structures and its application. (a) 2D design of micro linker structure (b) a printed linker structure (c) zoomed-in view of locking hooks in linker structure (d) a silicon delay line supported by foam blocks without linker structure (e) a silicon delay line supported by foam blocks with four linker structures [86]. Reprinted with permission © 2016 by JMM.

The silicon acoustic delay line was fabricated in a 280μm-thick unpolished silicon wafer (University Wafers, Boston, MA, USA). A 300-nm thick aluminum layer was deposited and patterned as the etch mask. The silicon delay line structure was formed in

the silicon wafer by using a cryogenic reactive ion etching process on PlasmaLab 100 Etcher (Oxford Instruments, Abingdon, UK). The process parameters for the reactive ion etching are listed in Table 7. Due to its complex 3D geometry, it is difficult to fabricate the micro linker structures using conventional microfabrication process. To address this issue, the micro linker structures were designed in Solidworks® first and directly printed out with a high-resolution 3D printer (Perfactory® Micro DDP, Envisiontec, Inc., Michigan, USA) with the highest resolution of ~30 μm. The 3D printing process is based on direct optical projection to cure photopolymer resin into 3D objects one layer at a time. Figure 35a shows the 2D design of the micro polymer linker structures. A printed linker structure and a zoomed-in view of the locking hooks are shown in Figures 35b and 35c, respectively. The fabricated delay line (without and with linkers), which was supported at both ends by two foam blocks, are shown in Figures 35d and 35e, respectively.

Table 7 Parameters used for the reactive ion etching [86]. Reprinted with permission © 2016 by JMM.

Parameters	Value
SF_6 / O_2	90 / 30 sccm
RF / ICP	30 / 1000 W
Process pressure	15 mT
Helium backing	35.5 sccm
Temperature	-100 °C
Time	90 min

5.3 Ultrasonic testing and results

5.3.1 Ultrasonic testing with straight silicon delay lines

Two-port ultrasound transmission testing was conducted to characterize the potential acoustic attenuation and coupling caused by the contact between silicon delay lines and the linker structures (Figure 36). A pulser/receiver (5072PR, Olympus NDT, Waltham, MA, USA) was connected to two 2.25 MHz ultrasound transducers (V104, Olympus NDT, Waltham, MA, USA) to transmit and receive the ultrasound signals. After being amplified by the pulser/receiver, the received ultrasound signals are displayed on the oscilloscope (TDS2002C, Tektronix Inc., Beaverton, OR, USA). Two delay line structures were tested, including a single straight silicon delay line supported by two linker structures and double straight silicon delay lines supported and separated by two linker structures. During the testing, both ends of the single straight silicon delay line were in contact with the transmitting and receiving transducers (Figure 37a). For the double straight silicon delay lines, only one end of each silicon delay line was in contact with the transmitting transducer and the receiving transducer, respectively (Figure 37b). Figure 37c shows the received ultrasound signal from the single straight silicon delay line. The first signal is the transmitted ultrasound signal and the second and third one are the first and second reflection signals. This result shows that the addition of linker structures do not cause significant acoustic attenuation in the transmission of the ultrasound signals through the silicon delay line. Figure 37d shows the received signal from the double straight silicon delay lines which indicates no notable ultrasound signal was detected. This result shows

that that the linker structures provided good acoustic isolation between two adjacent delay lines.

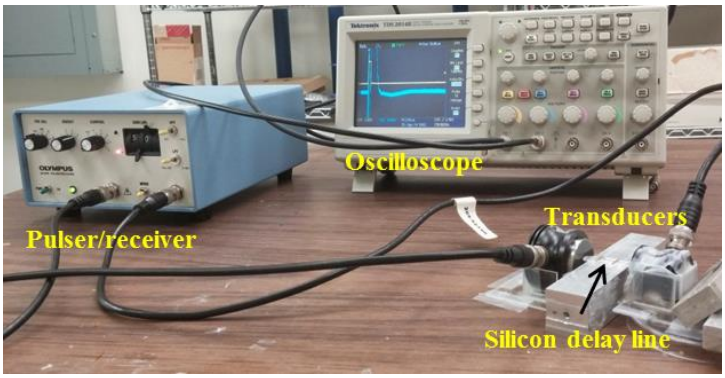

Figure 36 Two port ultrasound experiment setup for silicon delay line with linker structures [86]. Reprinted with permission © 2016 by JMM.

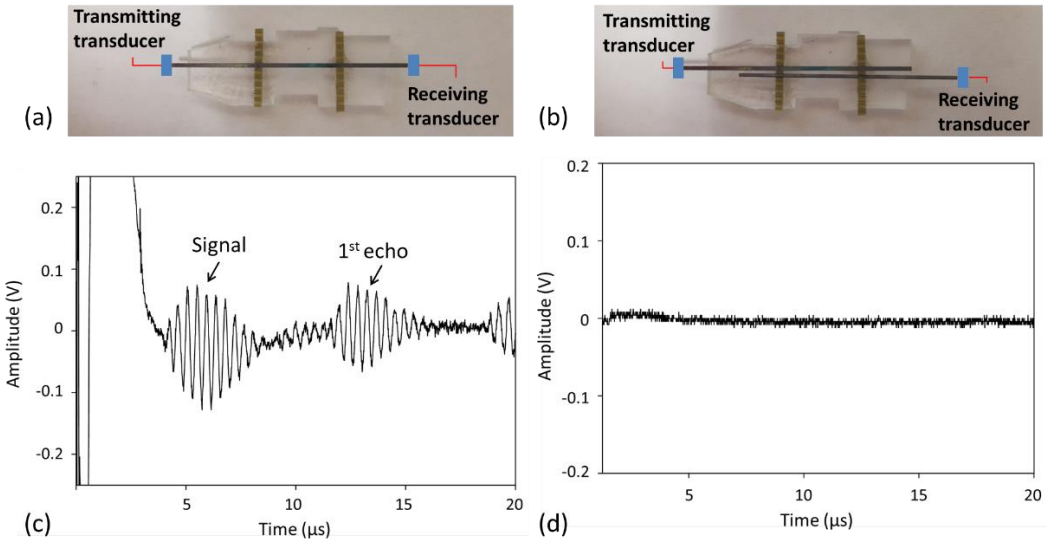

Figure 37 Ultrasound transmission testing results (a) through a straight silicon delay line supported on two linker structures, (b) through two straight silicon delay lines isolated by two linker structures, (c) acoustic signal received by the receiving transducer of (a), (d) acoustic signal received by the receiving transducer of (b) [86]. Reprinted with permission © 2016 by JMM.

5.3.2 Ultrasonic testing with the long silicon delay line

Ultrasound transmission testing was conducted with the fabricated long silicon delay line with and without the linker structures. First, both ends of the long silicon delay line (without linker structures) were supported on foam blocks. Its input terminal (with a tapered end) was contacted with the transmitting transducer and its output terminal was contacted with the receiving transducer. No ultrasound signal can be transmitted through this delay line structure because it has collapsed under its own weight (Figure 38a). Second, the delay line (without linker structures) was laid flat on a piece of foam block to avoid the excessive deformation caused by its own weight The ultrasound signal transmitted through the delay line was acquired (Figure 38b). After this, four linker structures were manually assembled by pushing the locking hooks into the spacing between two adjacent turns. Both ends of the long silicon delay line (without linker structures) were supported on foam blocks. The ultrasound transmission testing was repeated (Figure 38c). As shown in Figures 38b and 38c, both transmitted ultrasound signals have similar pulse shape and peak amplitude with a total delay time of 192 μs, which is close to the designed value of 186 μs. This result clearly shows that the application of the four linker structures has little effect on the acoustic transmission of the silicon delay line.

5.4 Conclusion

In this paper, we have demonstrated an improved long silicon delay line with a wide input terminal and 3D printed micro linker structures. By using 3D-printed micro linker structures, the structural instability issue of the long silicon delay line structure caused by its low mechanical stiffness was eliminated without notable degradation in its

acoustic transmission properties. Numerical simulation results also demonstrated that smaller acoustic acceptance angle was achieved by enlarging the size of the input terminal. In the future, micromachined silicon delay line arrays with larger number of channels will be investigated to achieve higher transducer/channel reduction ratios for further reducing the complexity of the ultrasound receiver systems for real-time photoacoustic tomography. Moreover, acoustic impedance matching at the input terminal will be investigated for better acoustic signal detection.

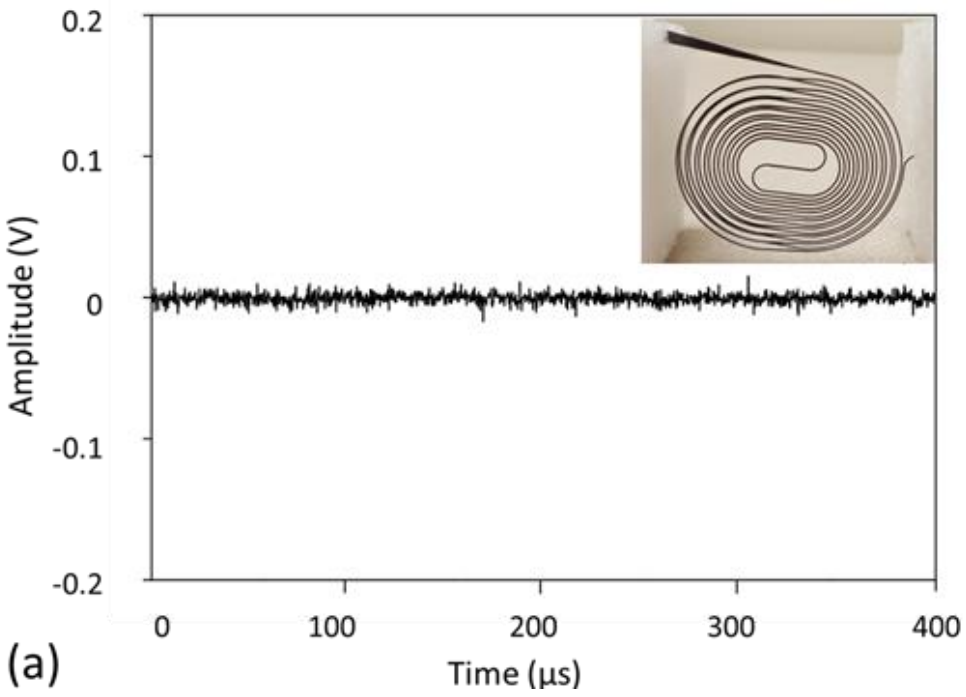

Figure 38 Ultrasound transmission testing results through a long silicon delay line (a) supported at both ends (without polymer linkers), (b) laid flat on a foam block (without polymer linkers), (c) supported at both ends (with polymer linkers) [86]. Reprinted with permission © 2016 by JMM.

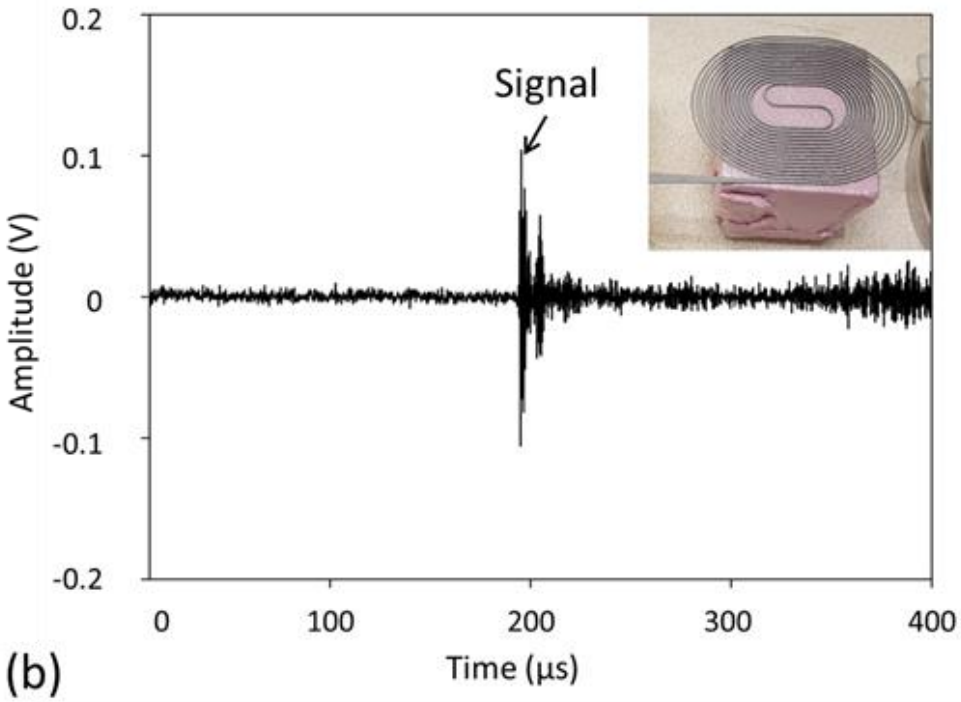

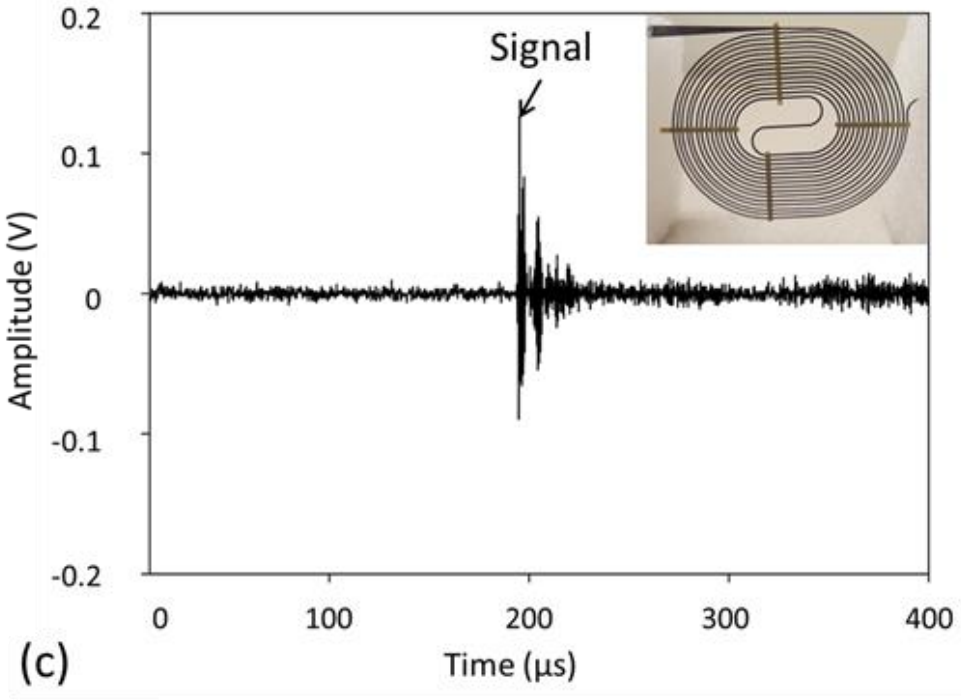

Figure 38 Continued.

6. CONCLUSIONS

In this study, the photoacoustic imaging capability of the micromachined optical fiber and silicon parallel acoustic delay line (PADL) arrays were demonstrated with ultrasonic transmission testing and photoacoustic imaging experiments. The micromachined PADL arrays have compact sizes for handheld operation. To develop micromachined optical fiber and silicon PADL arrays, the following steps were required: (1) calculation of acoustic time delay (length of delay line), (2) fabrication, (3) probe assembly, (4) ultrasonic transmission testing, and (5) photoacoustic imaging experiment. The optical fiber PADL array employed a laser-micromachined acrylic housing structure to hold multiple fibers securely in a compact space. Four pairs of crossed spacers allowed optical fibers to be threaded without breaking and excessive acoustic attenuation. Sixteen channels of optical fibers require two ultrasonic transducers which correspond to a channel reduction ratio of 8:1.

Micromachined silicon PADL array has been developed to address the issues of optical fiber PADL array. Silicon is a superior to optical fibers in terms of low acoustic attenuation, well-established microfabrication process, and mass production. Even if the speed of sound in silicon is faster than that in optical fiber, a transducer/channel reduction ratio of 16:1 was achieved due to the advantage of microfabrication process. Before constructing PADL array, acoustic properties of silicon was characterized by ultrasonic transmission testing. After material characterization, silicon PADLs were fabricated by

microfabrication process such as metal deposition, photolithography, wet etching, and deep reactive ion etching (DRIE).

For a larger number of PADL arrays with a high channel reduction ratio, as the number of channels increases, the structural stability decreases due to its own weight. By designing linker structures to support silicon PADLs, both structural and acoustic simulations for silicon delay line with linkers were conducted. Based on the simulation results, 3D-printed micro linker structure was designed and fabricated by a high-resolution 3D printer. 3D-printed micro linker structures improve the mechanical stability of long silicon acoustic delay lines and have minimal effect on the acoustic transmission. Tapered input terminal design was introduced and simulated for better spatial resolution.

Through parallel acoustic delay line arrays discussed in this thesis, the optical and silicon PADL arrays provided a new concept for handheld and low-cost real-time photoacoustic imaging system by reducing the number of hardware. By using different materials for a delay line, the PADL arrays can be applied to various research fields.

REFERENCES

[1] Wang X, Pang Y, Ku G, Xie X, Stoica G and Wang L V 2003 Noninvasive laser-induced photoacoustic tomography for structural and functional in vivo imaging of the brain *Nature biotechnology* **21** 803-06

[2] Li L, Zemp R J, Lungu G, Stoica G and Wang L V 2007 Photoacoustic imaging of lacZ gene expression in vivo *Journal of biomedical optics* **12** 020504-04-3

[3] Li M-L, Oh J-T, Xie X, Ku G, Wang W, Li C, Lungu G, Stoica G and Wang L V 2008 Simultaneous molecular and hypoxia imaging of brain tumors in vivo using spectroscopic photoacoustic tomography *Proceedings of the IEEE* **96** 481-89

[4] Xu M and Wang L V 2002 Time-domain reconstruction for thermoacoustic tomography in a spherical geometry *IEEE transactions on medical imaging* **21** 814-22

[5] Morgner U, Drexler W, Kärtner F, Li X, Pitris C, Ippen E and Fujimoto J 2000 Spectroscopic optical coherence tomography *Optics letters* **25** 111-13

[6] Grinvald A, Frostig R, Lieke E and Hildesheim R 1988 Optical imaging of neuronal activity *Physiological reviews* **68** 1285-366

[7] Frostig R D, Lieke E E, Ts'o D Y and Grinvald A 1990 Cortical functional architecture and local coupling between neuronal activity and the microcirculation revealed by in vivo high-resolution optical imaging of intrinsic signals *Proceedings of the National Academy of Sciences* **87** 6082-86

[8] MacVicar B A and Hochman D 1991 Imaging of synaptically evoked intrinsic optical signals in hippocampal slices *Journal of Neuroscience* **11** 1458-69

[9] Ebner T J and Chen G 1995 Use of voltage-sensitive dyes and optical recordings in the central nervous system *Progress in neurobiology* **46** 463-506

[10] Villringer A and Chance B 1997 Non-invasive optical spectroscopy and imaging of human brain function *Trends in neurosciences* **20** 435-42

[11] Gratton G and Fabiani M 1998 Dynamic brain imaging: Event-related optical signal (EROS) measures of the time course and localization of cognitive-related activity *Psychonomic Bulletin & Review* **5** 535-63

[12] Grinvald A, Lieke E, Frostig R D, Gilbert C D and Wiesel T N 1986 Functional architecture of cortex revealed by optical imaging of intrinsic signals

[13] Haglund M M, Ojemann G A and Hochman D W 1992 Optical imaging of epileptiform and functional activity in human cerebral cortex *Nature* **358** 668

[14] Dowling J L, Henegar M M, Liu D, Rovainen C M and Woolsey T A 1996 Rapid optical imaging of whisker responses in the rat barrel cortex *Journal of neuroscience methods* **66** 113-22

[15] Jones M, Berwick J and Mayhew J 2002 Changes in blood flow, oxygenation, and volume following extended stimulation of rodent barrel cortex *Neuroimage* **15** 474-87

[16] Hoelen C, De Mul F, Pongers R and Dekker A 1998 Three-dimensional photoacoustic imaging of blood vessels in tissue *Optics letters* **23** 648-50

[17] Kruger R A, Reinecke D R and Kruger G A 1999 Thermoacoustic computed tomography–technical considerations *Medical physics* **26** 1832-37

[18] Esenaliev R O, Karabutov A A and Oraevsky A A 1999 Sensitivity of laser opto-acoustic imaging in detection of small deeply embedded tumors *IEEE Journal of Selected Topics in Quantum Electronics* **5** 981-88

[19] Paltauf G, Schmidt-Kloiber H, Köstli K and Frenz M 1999 Optical method for two-dimensional ultrasonic detection *Applied Physics Letters* **75** 1048-50

[20] Karabutov A A, Savateeva E V, Podymova N B and Oraevsky A A 2000 Backward mode detection of laser-induced wide-band ultrasonic transients with optoacoustic transducer *Journal of Applied Physics* **87** 2003-14

[21] Kostli K, Frauchiger D, Niederhauser J J, Paltauf G, Weber H P and Frenz M 2001 Optoacoustic imaging using a three-dimensional reconstruction algorithm *IEEE Journal of Selected Topics in Quantum Electronics* **7** 918-23

[22] Wang X, Xu Y, Xu M, Yokoo S, Fry E S and Wang L V 2002 Photoacoustic tomography of biological tissues with high cross-section resolution: Reconstruction and experiment *Medical physics* **29** 2799-805

[23] Tokuno H, Hatanaka N, Takada M and Nambu A 2000 B-mode and color Doppler ultrasound imaging for localization of microelectrode in monkey brain *Neuroscience research* **36** 335-38

[24] Wang L and Wu H-i Biomedical optics: principles and imaging. 2007, Hoboken. NJ: Wiley-Interscience. xiv)

[25] Ermilov S A, Khamapirad T, Conjusteau A, Leonard M H, Lacewell R, Mehta K, Miller T and Oraevsky A A 2009 Laser optoacoustic imaging system for detection of breast cancer *Journal of biomedical optics* **14** 024007-07-14

[26] Pramanik M, Ku G, Li C and Wang L V 2008 Design and evaluation of a novel breast cancer detection system combining both thermoacoustic (TA) and photoacoustic (PA) tomography *Medical physics* **35** 2218-23

[27] Ku G, Fornage B D, Jin X, Xu M, Hunt K K and Wang L V 2005 Thermoacoustic and photoacoustic tomography of thick biological tissues toward breast imaging *Technology in cancer research & treatment* **4** 559-65

[28] Piras D, Xia W, Steenbergen W, van Leeuwen T G and Manohar S 2010 Photoacoustic imaging of the breast using the twente photoacoustic mammoscope: present status and future perspectives *IEEE Journal of Selected Topics in Quantum Electronics* **16** 730-39

[29] Manohar S, Vaartjes S E, van Hespen J C, Klaase J M, van den Engh F M, Steenbergen W and Van Leeuwen T G 2007 Initial results of in vivo non-invasive cancer imaging in the human breast using near-infrared photoacoustics *Optics express* **15** 12277-85

[30] Manohar S, Kharine A, van Hespen J C, Steenbergen W and van Leeuwen T G 2004 Photoacoustic mammography laboratory prototype: imaging of breast tissue phantoms *Journal of biomedical optics* **9** 1172-81

[31] Kumavor P D, Xu C, Aguirre A, Gamelin J, Ardeshirpour Y, Tavakoli B, Zanganeh S, Alqasemi U, Yang Y and Zhu Q 2011 Target detection and quantification using a hybrid hand-held diffuse optical tomography and photoacoustic tomography system *Journal of biomedical optics* **16** 046010-10-12

[32] Ku G, Wang X, Stoica G and Wang L V 2004 Multiple-bandwidth photoacoustic tomography *Physics in medicine and biology* **49** 1329

[33] Zhang H F, Maslov K, Stoica G and Wang L V 2006 Functional photoacoustic microscopy for high-resolution and noninvasive in vivo imaging *Nature biotechnology* **24** 848-51

[34] Zhang H F, Maslov K and Wang L V 2009 Automatic algorithm for skin profile detection in photoacoustic microscopy *Journal of biomedical optics* **14** 024050-50-6

[35] Xu M and Wang L V 2005 Universal back-projection algorithm for photoacoustic computed tomography *Physical Review E* **71** 016706

[36] Xu M and Wang L V 2006 Photoacoustic imaging in biomedicine *Review of scientific instruments* **77** 041101

[37] Wang X, Xie X, Ku G, Wang L V and Stoica G 2006 Noninvasive imaging of hemoglobin concentration and oxygenation in the rat brain using high-resolution photoacoustic tomography *Journal of biomedical optics* **11** 024015-15-9

[38] Yang S, Xing D, Zhou Q, Xiang L and Lao Y 2007 Functional imaging of cerebrovascular activities in small animals using high-resolution photoacoustic tomography *Medical physics* **34** 3294-301

[39] Lao Y, Xing D, Yang S and Xiang L 2008 Noninvasive photoacoustic imaging of the developing vasculature during early tumor growth *Physics in medicine and biology* **53** 4203

[40] Ma R, Taruttis A, Ntziachristos V and Razansky D 2009 Multispectral optoacoustic tomography (MSOT) scanner for whole-body small animal imaging *Optics express* **17** 21414-26

[41] Razansky D, Vinegoni C and Ntziachristos V 2009 Imaging of mesoscopic-scale organisms using selective-plane optoacoustic tomography *Physics in medicine and biology* **54** 2769

[42] Razansky D, Distel M, Vinegoni C, Ma R, Perrimon N, Köster R W and Ntziachristos V 2009 Multispectral opto-acoustic tomography of deep-seated fluorescent proteins in vivo *Nature Photonics* **3** 412-17

[43] Laufer J, Johnson P, Zhang E, Treeby B, Cox B, Pedley B and Beard P 2012 In vivo preclinical photoacoustic imaging of tumor vasculature development and therapy *Journal of biomedical optics* **17** 0560161-68

[44] Heijblom M, Piras D, Xia W, Van Hespen J, Klaase J, Van den Engh F, Van Leeuwen T, Steenbergen W and Manohar S 2012 Visualizing breast cancer using the Twente photoacoustic mammoscope: what do we learn from twelve new patient measurements? *Optics express* **20** 11582-97

[45] Su R, Ermilov S A, Liopo A V and Oraevsky A A 2012 Three-dimensional optoacoustic imaging as a new noninvasive technique to study long-term biodistribution of optical contrast agents in small animal models *Journal of biomedical optics* **17** 1015061-67

[46] Paltauf G, Nuster R and Burgholzer P 2009 Weight factors for limited angle photoacoustic tomography *Physics in medicine and biology* **54** 3303

[47] Hu S, Maslov K and Wang L V 2009 Noninvasive label-free imaging of microhemodynamics by optical-resolution photoacoustic microscopy *Optics express* **17** 7688-93

[48] Yang D, Xing D, Tan Y, Gu H and Yang S 2006 Integrative prototype B-scan photoacoustic tomography system based on a novel hybridized scanning head *Applied physics letters* **88** 174101

[49] Yang D, Xing D, Yang S and Xiang L 2007 Fast full-view photoacoustic imaging by combined scanning with a linear transducer array *Optics Express* **15** 15566-75

[50] Allen T J and Beard P C 2006 Pulsed near-infrared laser diode excitation system for biomedical photoacoustic imaging *Optics letters* **31** 3462-64

[51] Maslov K, Zhang H F and Wang L V 2007 Portable real-time photoacoustic microscopy. In: *Biomedical Optics (BiOS) 2007*, International Society for Optics and Photonics) pp 643727-27-7

[52] Erpelding T N, Kim C, Pramanik M, Jankovic L, Maslov K, Guo Z, Margenthaler J A, Pashley M D and Wang L V 2010 Sentinel lymph nodes in the rat: noninvasive photoacoustic and US imaging with a clinical US system 1 *Radiology* **256** 102-10

[53] Gamelin J, Aguirre A, Maurudis A, Huang F, Castillo D, Wang L V and Zhu Q 2008 Curved array photoacoustic tomographic system for small animal imaging *Journal of biomedical optics* **13** 024007-07-10

[54] Gamelin J, Maurudis A, Aguirre A, Huang F, Guo P, Wang L V and Zhu Q 2009 A real-time photoacoustic tomography system for small animals *Optics express* **17** 10489-98

[55] Jetzfellner T, Rosenthal A, Buehler A, Englmeier K-H, Razansky D and Ntziachristos V 2011 Multispectral optoacoustic tomography by means of normalized spectral ratio *Optics letters* **36** 4176-78

[56] Kim C, Erpelding T N, Jankovic L, Pashley M D and Wang L V 2010 Deeply penetrating in vivo photoacoustic imaging using a clinical ultrasound array system *Biomedical optics express* **1** 278-84

[57] Kim C, Erpelding T N, Jankovic L and Wang L V 2011 Performance benchmarks of an array-based hand-held photoacoustic probe adapted from a clinical ultrasound system for non-invasive sentinel lymph node imaging *Philosophical Transactions of the Royal Society of London A: Mathematical, Physical and Engineering Sciences* **369** 4644-50

[58] Kim C, Erpelding T N, Maslov K, Jankovic L, Akers W J, Song L, Achilefu S, Margenthaler J A, Pashley M D and Wang L V 2010 Handheld array-based photoacoustic probe for guiding needle biopsy of sentinel lymph nodes *Journal of biomedical optics* **15** 046010-10-4

[59] Xia J and Wang L V 2014 Small-animal whole-body photoacoustic tomography: a review *IEEE Transactions on Biomedical Engineering* **61** 1380-89

[60] Xia J, Chatni M R, Maslov K, Guo Z, Wang K, Anastasio M and Wang L V 2012 Whole-body ring-shaped confocal photoacoustic computed tomography of small animals in vivo *Journal of biomedical optics* **17** 0505061-63

[61] Tang J, Coleman J, Dai X and Jiang H 2016 3-D Photoacoustic Tomography Brain Imaging in Behaving Animal. In: *Optical Tomography and Spectroscopy*, Optical Society of America) p OM2C. 3

[62] Yao J, Xia J, Maslov K I, Nasiriavanaki M, Tsytsarev V, Demchenko A V and Wang L V 2013 Noninvasive photoacoustic computed tomography of mouse brain metabolism in vivo *Neuroimage* **64** 257-66

[63] Li C, Aguirre A, Gamelin J, Maurudis A, Zhu Q and Wang L V 2010 Real-time photoacoustic tomography of cortical hemodynamics in small animals *Journal of biomedical optics* **15** 010509-09-3

[64] Yin B, Xing D, Wang Y, Zeng Y, Tan Y and Chen Q 2004 Fast photoacoustic imaging system based on 320-element linear transducer array *Physics in medicine and biology* **49** 1339

[65] Xiang L, Ji L, Zhang T, Wang B, Yang J, Zhang Q, Jiang M S, Zhou J, Carney P R and Jiang H 2013 Noninvasive real time tomographic imaging of epileptic foci and networks *Neuroimage* **66** 240-48

[66] Buehler A, Deán-Ben X, Claussen J, Ntziachristos V and Razansky D 2012 Three-dimensional optoacoustic tomography at video rate *Optics express* **20** 22712-19

[67] Kruger R A, Kiser W L, Reinecke D R and Kruger G A 2003 Thermoacoustic computed tomography using a conventional linear transducer array *Medical physics* **30** 856-60

[68] Oraevsky A A, Karabutov A A, Solomatin S V, Savateeva E V, Andreev V A, Gatalica Z, Singh H and Fleming R D 2001 Laser optoacoustic imaging of breast cancer in vivo. In: *BiOS 2001 The International Symposium on Biomedical Optics*, International Society for Optics and Photonics) pp 6-15

[69] Zhou Q, Ji X and Xing D 2011 Full-field 3D photoacoustic imaging based on plane transducer array and spatial phase-controlled algorithm *Medical physics* **38** 1561-66

[70] Olafsson R, Bauer D R, Montilla L G and Witte R S 2010 Real-time, contrast enhanced photoacoustic imaging of cancer in a mouse window chamber *Optics express* **18** 18625-32

[71] Taruttis A, Herzog E, Razansky D and Ntziachristos V 2010 Real-time imaging of cardiovascular dynamics and circulating gold nanorods with multispectral optoacoustic tomography *Optics Express* **18** 19592-602

[72] Kolkman R G, Brands P J, Steenbergen W and van Leeuwen T G 2008 Real-time in vivo photoacoustic and ultrasound imaging *Journal of biomedical optics* **13** 050510-10-3

[73] Yuan J, Xu G, Yu Y, Zhou Y, Carson P L, Wang X and Liu X 2013 Real-time photoacoustic and ultrasound dual-modality imaging system facilitated with graphics processing unit and code parallel optimization *Journal of biomedical optics* **18** 086001-01

[74] Guo H and Yang S 2009 Photoacoustic tomography imaging system based on digital B-mode ultrasound diagnosis equipment *Review of Scientific Instruments* **80** 014903

[75] Song K H and Wang L V 2008 Noninvasive photoacoustic imaging of the thoracic cavity and the kidney in small and large animals *Medical physics* **35** 4524-29

[76] Nie L, Xing D, Yang D, Zeng L and Zhou Q 2007 Detection of foreign body using fast thermoacoustic tomography with a multielement linear transducer array *Applied physics letters* **90** 174109

[77] Auerbach I L, Eckert J P, Shaw R F and Sheppard C B 1949 Mercury delay line memory using a pulse rate of several megacycles *Proceedings of the IRE* **37** 855-61

[78] Arenberg D L 1948 Ultrasonic solid delay lines *The Journal of the Acoustical Society of America* **20** 1-26

[79] May J 1960 Wire-type dispersive ultrasonic delay lines *IRE Transactions on Ultrasonic Engineering* **7** 44-52

[80] Boyd G, Coldren L and Thurston R 1977 Acoustic clad fiber delay lines *IEEE Transactions on Sonics and Ultrasonics* **24** 246-52

[81] Moriya T, Hu Z and Tanahashi Y 2000 Development of flexible acoustic transmission line for intravascular ultrasonography. In: *Ultrasonics Symposium, 2000 IEEE*, IEEE) pp 1227-30

[82] Yapici M K, Kim C, Chang C-C, Jeon M, Guo Z, Cai X, Zou J and Wang L V 2012 Parallel acoustic delay lines for photoacoustic tomography *Journal of biomedical optics* **17** 116019-19

[83] Cho Y, Chang C-C, Yu J, Jeon M, Kim C, Wang L V and Zou J 2014 Handheld photoacoustic tomography probe built using optical-fiber parallel acoustic delay lines *Journal of biomedical optics* **19** 086007-07

[84] Cho Y, Chang C, Wang L and Zou J 2016 Micromachined silicon parallel acoustic delay lines as time-delayed ultrasound detector array for real-time photoacoustic tomography *Journal of Optics* **18** 024003

[85] Cho Y, Chang C-C, Wang L V and Zou J 2015 A micromachined silicon parallel acoustic delay line (PADL) array for real-time photoacoustic tomography (PAT). In: *SPIE BiOS*, International Society for Optics and Photonics) pp 93232Z-32Z-5

[86] Cho Y, Kumar A, Xu S and Zou J 2016 Micromachined silicon acoustic delay line with 3D-printed micro linkers and tapered input for improved structural stability and acoustic directivity *Journal of Micromechanics and Microengineering* **26** 105003

[87] Fronheiser M P, Ermilov S A, Brecht H-P, Conjusteau A, Su R, Mehta K and Oraevsky A A 2010 Real-time optoacoustic monitoring and three-dimensional mapping of a human arm vasculature *Journal of biomedical optics* **15** 021305-05-7

[88] Song L, Kim C, Maslov K, Shung K K and Wang L V 2009 High-speed dynamic 3D photoacoustic imaging of sentinel lymph node in a murine model using an ultrasound array *Medical physics* **36** 3724

[89] Auld B A 1973 *Acoustic fields and waves in solids* vol 1 (New York: Wiley)

[90] Meeker T 1960 Dispersive ultrasonic delay lines using the first longitudinal mode in a strip *Ultrasonic Engineering, IRE Transactions on* **7** 53-58

[91] Cheeke J D N 2012 *Fundamentals and applications of ultrasonic waves* (New York: CRC press)

[92] Rosencwaig A and Gersho A 1976 Theory of the photoacoustic effect with solids *Journal of Applied Physics* **47** 64-69

[93] Chang C-C, Cho Y, Wang L and Zou J 2013 Micromachined silicon acoustic delay lines for ultrasound applications *Journal of Micromechanics and Microengineering* **23** 025006

[94] May J 1960 Wire-type dispersive ultrasonic delay lines *Ultrasonic Engineering, IRE Transactions on* **7** 44-52

[95] Gelles I 1966 Optical-Fiber Ultrasonic Delay Lines *The Journal of the Acoustical Society of America* **39** 1111

[96] Beranek L L and Mellow T 2012 *Acoustics: sound fields and transducers* (Waltham, MA: Academic Press)

[97] Ylitalo J T and Ermert H 1994 Ultrasound synthetic aperture imaging: monostatic approach *Ultrasonics, Ferroelectrics and Frequency Control, IEEE Transactions on* **41** 333-39

[98] Schechter R, Chaskelis H, Mignogna R and Delsanto P 1994 Real-time parallel computation and visualization of ultrasonic pulses in solids *Science* **265** 1188-92

[99] Zhou S, Wojcik G L and Hossack J A 2003 An approach for reducing adjacent element crosstalk in ultrasound arrays *IEEE transactions on ultrasonics, ferroelectrics, and frequency control* **50** 1752-61

[100] Carson J R 1924 A generalization of the reciprocal theorem *Bell System Technical Journal, The* **3** 393-99

[101] Li C, Ku G and Wang L V 2008 Negative lens concept for photoacoustic tomography *Physical Review E* **78** 021901

[102] Xia W, Piras D, van Hespen J C, Steenbergen W and Manohar S 2013 A new acoustic lens material for large area detectors in photoacoustic breast tomography *Photoacoustics* **1** 9-18